Molecular beam scattering studies of orbiting resonances and the determination of van der Waals potentials for H–Ne, Ar, Kr, and Xe and for H2–Ar, Kr, and Xe

J. Peter Toennies, Wolfgang Welz, and Günther Wolf

Citation: J. Chem. Phys. **71**, 614 (1979); doi: 10.1063/1.438414
View online: http://dx.doi.org/10.1063/1.438414
View Table of Contents: http://jcp.aip.org/resource/1/JCPSA6/v71/i2
Published by the American Institute of Physics.

Molecular beam scattering studies of orbiting resonances and the determination of van der Waals potentials for H–Ne, Ar, Kr, and Xe and for H_2–Ar, Kr, and Xe

J. Peter Toennies, Wolfgang Welz,[a] and Günther Wolf[b]

Max-Planck-Institut für Strömungsforschung, Böttinger Str. 4–8, 3400 Göttingen, Federal Republic of Germany

(Received 21 November 1978)

The velocity dependence of the integral cross sections for the scattering of H atoms and normal-H_2 molecules from the rare gases has been measured for primary beam velocities from 300 m/sec ($E_{c.m.} = 0.5$ meV) to about 3000 m/sec ($E_{c.m.} = 100$ meV). Three distinct resonance maxima were observed in each of the systems H–Xe, H–Kr, H_2–Kr, and H_2–Ar. At least one resonance maximum was found in H_2–Xe and H–Ar, while H–Ne showed no maxima. The H_2–Ar cross sections were also measured with a cold beam of pure para-H_2 consisting entirely of spherically symmetric $j = 0$ molecules. No noticeable difference was found when compared to the n-H_2 cross sections indicating that the observed resonances depend only on the spherical symmetric potential. Extensive comparisons with spherical symmetric model potentials showed that all the observed resonances are due to temporary capture in the well of the effective potential. This phenomenon is usually referred to as "orbiting". The energetic location of the observed orbiting resonances and glory maxima were found to be very sensitive to the potential shapes and parameters. Only models which included at least two terms in the long range dispersion potential C_6/R^6 and C_8/R^8, could describe the data in a satisfactory way. For H–Ar the data are in very good agreement with the experimental potential of Bassi *et al.* and in reasonable agreement with the *ab initio* MCSF potential of Wagner *et al.* For H_2–Ar, –Kr, –Xe good agreement is found with the potentials recently determined from infrared spectra by Le Roy and co-workers. For all the other systems new best fit potentials have been determined. The best fit values of ϵ and R_m are for H–Ne: 1.90 meV and 3.15 Å; H–Ar: 4.16 meV and 3.62 Å; H–Kr: 5.90 meV and 3.57 Å; H–Xe: 7.08 meV and 3.82 Å; H_2–Ar: 6.30 meV and 3.57 Å; H_2–Kr: 7.19 meV and 3.72 Å, and H_2–Xe: 8.10 meV and 3.92 Å.

I. INTRODUCTION

Orbiting resonances are prominent usually sharp extrema in the velocity dependence of integral scattering cross sections. They are attributed to a resonant coupling of a narrow energy band of translational states having a given orbital angular momentum quantum number, with quasibound vibrational states of the molecule temporarily formed during the collision. Related resonances are well known in electron scattering and nuclear physics, where they are frequently referred to as shape resonances. Only recently however have they been directly observed in the very low energy scattering of atoms and molecules. Although in principle the extrema may either appear as maxima or minima, in all the atom scattering experiments performed so far they have been observed to be maxima.

Orbiting and related scattering resonance phenomena are of great interest for understanding the recombination of atoms and molecules in the gas phase. Already in 1898 Boltzmann[1] postulated that gas phase recombination proceeded by the following mechanism

$$X + X \rightarrow X_2^* \tag{1a}$$

$$X_2^* + M \rightarrow X_2 + M\,, \tag{1b}$$

where X_2^* is an intermediate and M is some collision partner, e. g., either X, X_2, or a third body. This idea was further developed by Herzfeld[2] (1922) and Steiner[3] (1932) and others.[4] However only in 1954 did Hirschfelder, Curtiss, and Bird[5] discuss quantitatively the process of classical orbiting. Quantum effects were first treated in 1959 by Ford *et al.*[6] In 1960 Bunker[7] was probably the first to identify the previously postulated gas phase recombination intermediates as classical orbiting resonances. Only recently has Bunker's theory been extended by Bernstein, Curtiss and coworkers[8] to take account of quantum effects in order to apply it to the recombination of H atoms. In addition to the "energy transfer" mechanisms of Eq. (1) modern theories of recombination invoke an additional so-called "chaperon" mechanism[8]

$$X + M \rightleftharpoons XM^* \tag{2a}$$

$$XM^* + X \rightarrow X_2 + M\,, \tag{2b}$$

where M is a third body and the second step is a chemical reaction.

In both mechanisms it is now generally recognized that a resonance process must be involved in order to lengthen the collision time by at least an order of magnitude and thereby increasing the probability of a second bimolecular collision leading to a stable diatomic molecule. Other resonant processes other than orbiting have also been shown to be of importance.[10] A number of attempts have been undertaken to predict measured low temperature H atom recombination rate constants.[8,9,11] Despite considerable work however it has still not been possible to predict rate constants even for this simple case.[12]

The role of quasibound collision intermediates has also been extensively studied in connection with the equation of state and the transport properties of gases

[a] Present address: Stockholmer Str. 12, 5300 Bonn.
[b] Present address: Im Tentefeld 20, 5064 Roesrath.

 0021-9606/79/020614-29$01.00

at low temperatures. [13] Recently resonant processes have also been shown to be important in low energy inelastic collisions[14] in which there is now great astrophysical interest.

Apparently largely unnoticed by gas kineticists resonance phenomena in the interaction of atoms in molecules had already been established in the 1920's by the spectroscopic observation of the inverse process of predissociation. [15] Most of the earlier spectroscopic observations were in the visible and involved chemically bound systems. Recently predissociation has also been seen in the infrared spectrum of van der Waals bound systems including H_2–Ar, Kr, and Xe. [16] In the past the observed predissociation lines have been used to determine the electronic states of atomic dissociation products, dissociation energies, and the shape of the long range potential. [17] Although quantitative methods have been developed for extracting the constants describing the long range attractive potential, it now appears unlikely that this data alone is sufficient to determine long range potential constants. [18a] Nevertheless these studies have demonstrated that predissociation and its inverse process, orbiting, provide the most sensitive experimental probe of the long range potential between atoms and molecules.

Despite their importance orbiting resonances have only recently been directly observed in molecular beam scattering[19] and ion beam[20] experiments. After a long search[21] several broad resonances were recently found in integral cross sections of H–Hg. [22] For this chemically bound system the resonances are expected to be very sharp and superimposed on an oscillating glory background making their identification and resolution difficult. Another complication arises because of an avoided curve crossing in the region of internuclear distances where the potential passes over from a pure van der Waals to a chemical interaction. [23] This leads to an apparent quenching of the resonances in the region of accessible collision energies. At about the same time well-resolved resonances in the low energy scattering of H and H_2 from the rare gases and the symmetric molecules CF_4 and SF_6 were observed in our laboratory. [24] More recently resonance maxima were also found by Skofronik and co-workers in He–Ne. [25] Because of the shallow wells ($\lesssim 6$ meV) of these van der Waals bound systems these resonances could only be observed at substantially smaller collision energies extending into the submillivolt range.

In this paper we report on the details of the apparatus and the data analysis used in the scattering studies of H and H_2 from the rare gases. In the next section we first review the theory of the orbiting resonances in order to establish the special requirements placed on the apparatus to make the observation of resonance maxima possible. The apparatus is discussed next. The cold H-atom beam source and the target nozzle beam geometry are described in considerable detail. In a following section the method of data analysis used to determine the spherical symmetric potentials for the scattering of H and H_2 from the rare gases is discussed. Finally, the best fit potentials for the systems H–Ne, H–Ar, H–Kr, H–Xe and H_2–Ar, H_2–Kr and H_2–Xe are presented and compared with other determinations and *ab initio* calculations. The paper closes with a brief summary and discussion.

II. THE PHYSICAL NATURE OF ORBITING RESONANCES

In the theoretical description of the scattering of two particles interacting by way of a spherical symmetric interaction potential $V_0(R)$ we can separate the rotational motion from the relative radial motion. Conservation of angular momentum requires that the rotational energy depends on the internuclear distance R and thus it is convenient to add this rotational energy to the potential to yield an effective potential

$$V_{\text{eff}}(l, R) = V_0(R) + \frac{\hbar^2 l(l+1)}{2\mu R^2} \quad , \tag{3}$$

where l is the orbital angular momentum quantum number and μ is the reduced mass. The second term is frequently called the centrifugal potential. The resulting effective potentials for one value of l for an assumed Lennard-Jones LJ (12, 6) potential for H–Kr are shown in Fig. 1. Note that for $l \neq 0$ the curves show maxima at intermediate R.

Physical insight into the phenomenon of orbiting is best obtained by consideration of classical scattering as illustrated by the trajectories shown in the insert in Fig. 1. In classical mechanics l will have continuous (nondiscrete) values. If for a given l the relative collision energy ($E_{\text{c.m.}} = \frac{1}{2}\mu g^2$, g is the relative velocity) equals the effective potential energy at one of the maxima then the radial energy will be zero at R_{max}, the location of the maximum in $V_{\text{eff}}(l, R)$. At this point all the relative energy is taken up by the rotational motion and the two atoms will rotate about each other without changing R. At slightly larger energies the atoms will be slowed at R_{max} but will speed up again at smaller R and finally be reflected at the classical turning point produced by the hard repulsive core. In this case the trajectory spirals about the hard core and is referred to as "orbiting." According to this classical picture orbiting can only occur for effective potentials exhibiting a maximum. For a LJ (12, 6) potential maxima are only present for $E_{\text{c.m.}} \leq 0.8\,\epsilon$, where ϵ is the well depth of $V(R)$[5].

At the low energies at which orbiting occurs we expect the De Broglie wave length to be large and especially for systems with small reduced masses the classical picture will not be correct. In addition to having discrete angular momenta, l, the vibrational levels of the well of the effective potential to the left of R_{max} will no longer be continuous. Thus for collision energies close to those of the maximum a resonance can occur between the translational energy $E_{\text{c.m.}}$ and a quasibound vibrational state. The width of the resonance will depend on the strength of the coupling, which for states with $E_{\text{c.m.}} \leq V_{\text{eff max}}$ determines the rate of tunneling through the barrier. Since the radial motion is also perturbed for $E_{\text{c.m.}} > V_{\text{eff max}}$ broad resonances will also occur here as well. We will refer to these as virtual quasibound resonances.

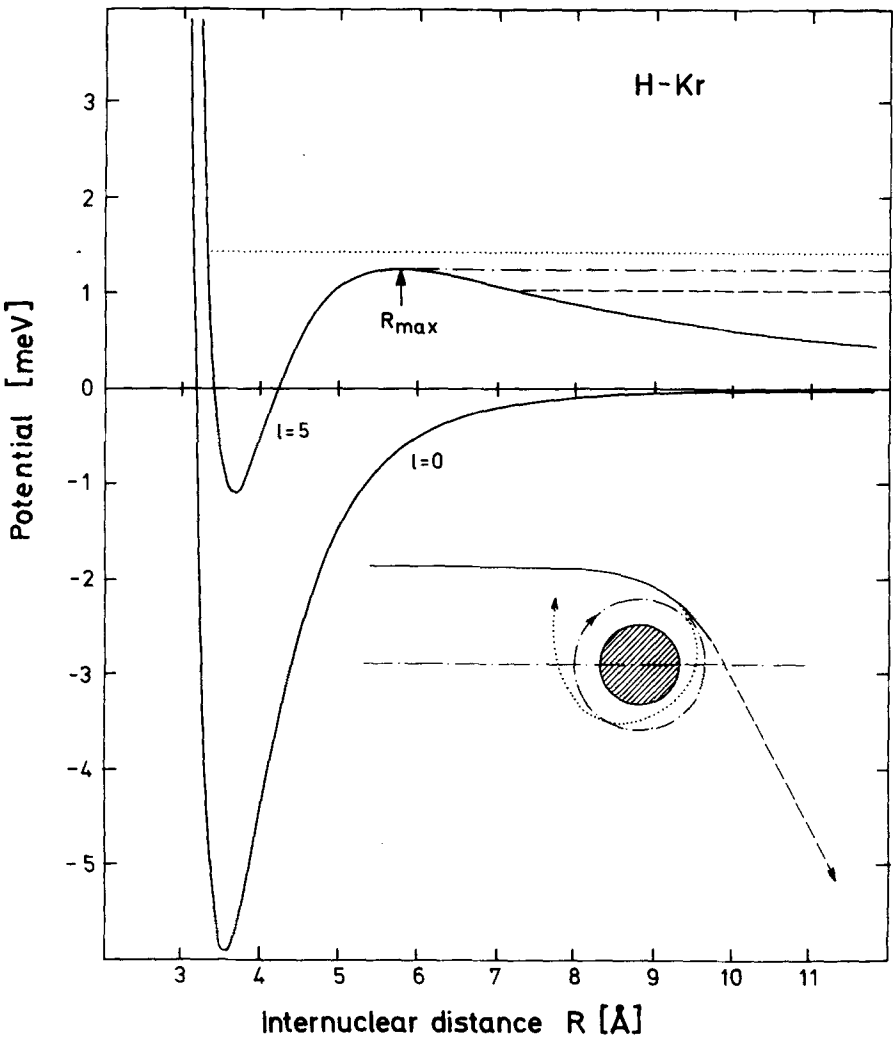

FIG. 1. The intermolecular potential of H–Kr and the effective potential for $l=5$ are plotted as a function of the internuclear distance for a Lennard-Jones (12,6) potential, The classical trajectories for the three energies indicated by the horizontal lines are shown in the insert.

Since the quantum mechanical theory of elastic cross sections and techniques for calculating these cross sections are well developed there is no difficulty in carrying out calculations of integral cross sections for a given potential. The expression for the integral cross section is particularly simple:

$$\sigma(k)=\frac{4\pi}{k^2}\sum_l \sigma_l(k)\ , \tag{4a}$$

where

$$\sigma_l(k)=(2l+1)\sin^2\eta_l(k)\ . \tag{4b}$$

Here k is the wave number ($E_{c.m.}=\hbar^2k^2/2\mu$), σ_l is the partial cross section, and η_l is the scattering phase for the lth partial wave. η_l is obtained from the asymptotic shift in the location of the radial wave function calculated for the given potential with respect to a wave function calculated without a potential. Figure 2 shows how the shape of the radial wave function changes with energy in the vicinity of a resonance. At resonance the amplitude in the minimum region increases drastically as the $n=0$ vibrational wave function is built up in the well region. Thus each time the energy passes through resonance the phase shift will change by π as an additional node is added. If the phase at an energy below a resonance is small then from Eq. (4b) we expect a maximum to appear in the partial cross section as η passes through $\pi/2$. Because of the differences in the effective potentials each partial wave will have its resonances at different energies. This is illustrated in Fig. 3(a), where the phase shifts are plotted for partial waves with $l=0$ to 6 over a wide range of collision energies. In Fig. 3(c) the corresponding partial cross sections σ_l and in Fig. 3(d) the observable sum of partial cross sections ($\sigma=\sum_l\sigma_l$) are shown as a function of E.

The half-width of a resonance is customarily given by

$$\Delta E=\frac{2}{\left(\frac{d\eta_l}{dE}\right)_{max}}\ . \tag{5}$$

The lifetime of a resonant state is obtained from the uncertainty principle $\tau=\hbar/\Delta E$. Due to the temporary capture into a quasibound state the time for a wave packet to pass through the potential is increased by an amount given by the time delay τ_d, which is defined by[26]

$$\tau_d(E)=2\hbar\left.\frac{d\eta_l(E)}{dE}\right|_{max}\ . \tag{6}$$

This is related to the lifetime τ by

$$\tau=\tfrac{1}{4}\tau_d\ . \tag{7}$$

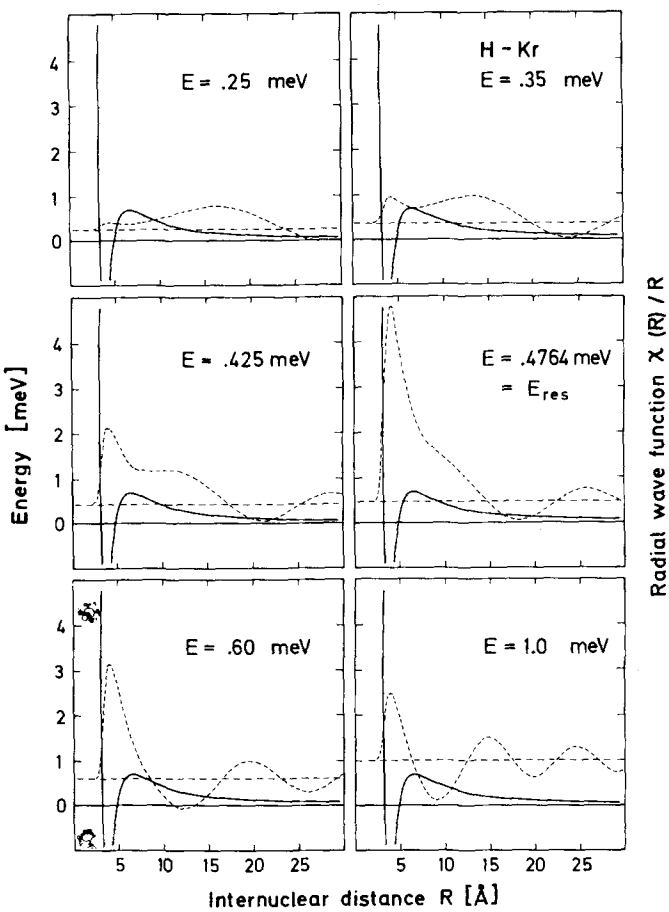

FIG. 2. The radial wave function $\chi(R)/R$ for the effective potential with $l=4$ is shown as a function of the internuclear distances for six different energies for H–Kr. At the resonance energy $E=0.4764$ meV corresponding to excitation of the $n=0$ quasibound vibrational level the wave function shows a large maximum in the well region indicating trapping of the H atom. Note that in going from 0.425 to 0.60 meV the wavefunction at large distances has added an additional node.

In the scattering of H atoms from the rare gas atoms the resonances have lifetimes of the order of 10^{-11} sec. These times may not appear large in comparison with the lifetimes of most complexes. However for these systems they represent an increase in the collision time of several orders of magnitude since the time delays outside of resonance are extremely small. This is clearly seen in Fig. 3(b) where the time delay outside the resonance is very small because of the only weak dependence of η on E outside the resonance region. Figure 4 summarizes the preceding discussion by showing the connection between the quantum mechanical cross sections (on the right) and the effective potentials and energy levels (on the left).

For heavy systems the number of partial waves and the number of resonances may become quite large. To cope with this situation a large number of papers have appeared in which the semiclassical method has been applied to study the resonances.[27] Much of this work is reviewed in Ref. 17. Because of the large de Broglie wavelength and small number of bound states involved in the results described here these approximations and related inversion procedures[18,28] are not directly applicable.

III. APPARATUS

The previous discussion indicates that an "ideal" apparatus should be able to measure integral cross sections down to collision energies less than 1 meV in the center of mass system. Furthermore in order to resolve the resonance maxima the relative half-width in the distribution of center of mass energies should be less than about 10% over the entire range of center of mass energies. Both these requirements could only be satisfied using a "converging" beam arrangement in which the primary beam is attenuated by a secondary beam which crosses the primary beam at an acute angle, which in this apparatus was 46°. In this arrangement the most probable relative velocity is given by

$$\hat{g}=v_0^2+\hat{u}^2-2v_0\hat{u}\cos\alpha\ , \tag{8}$$

where v_0 is the selected primary beam velocity and u the target beam velocity and $\hat{}$ stands for the most probable values of the respective distributions. α is the angle of intersection. Two advantages of this arrangement can be seen immediately. First and foremost the relative velocity for given v_0 and $\hat{u}$ is reduced by the amount of $2v_0\hat{u}\cos\alpha$ over the conventional crossed beam arrangement with $\alpha=90°$. In the conventional arrangement $\hat{g}$ can never be smaller than $\hat{u}$, which can be a severe limitation. In the converging beam arrangement $\hat{g}$ can be made arbitrarily small by reducing α without reducing v and $\hat{u}$. For a given α the minimum value of g is

$$\hat{g}_{\min}=\hat{u}\sin\alpha \tag{9}$$

for which

$$\frac{v_0}{\hat{u}}=\cos\alpha\ . \tag{10}$$

Thus for a small α v_0 approaches u at $g_{\min}$ and thus greater values of v_0, with correspondingly greater intensities than in the conventional apparatus, may be used. The second advantage has to do with the relative velocity smearing dg/g. For small α dg/g becomes less dependent on the spread in the two beams, but does become more sensitive on the spread in α. For not too small values of α this trade off also means greater intensities for a given value of dg/g.

The apparatus is shown in a schematic side view (roughly to scale) in Fig. 5(a) and briefly described next. The primary H-atom beam is produced in a discharge source. The temperature in the discharge is about 400 °K. Before leaving the source the temperature of the atoms is reduced by collisions with the walls of a short liquid N_2 cooled cylinder mounted between the discharge region and the exit slit. This cylinder thus serves as a "moderator." The Maxwellian H-atom beam is then velocity selected by a Fizeau-type mechanical velocity selector ($\Delta v/v=5.7\%$ FWHM) before entering the interaction region where it is crossed by the nozzle target beam with a velocity spread of less than 10%. The primary beam is detected by an electron bombardment

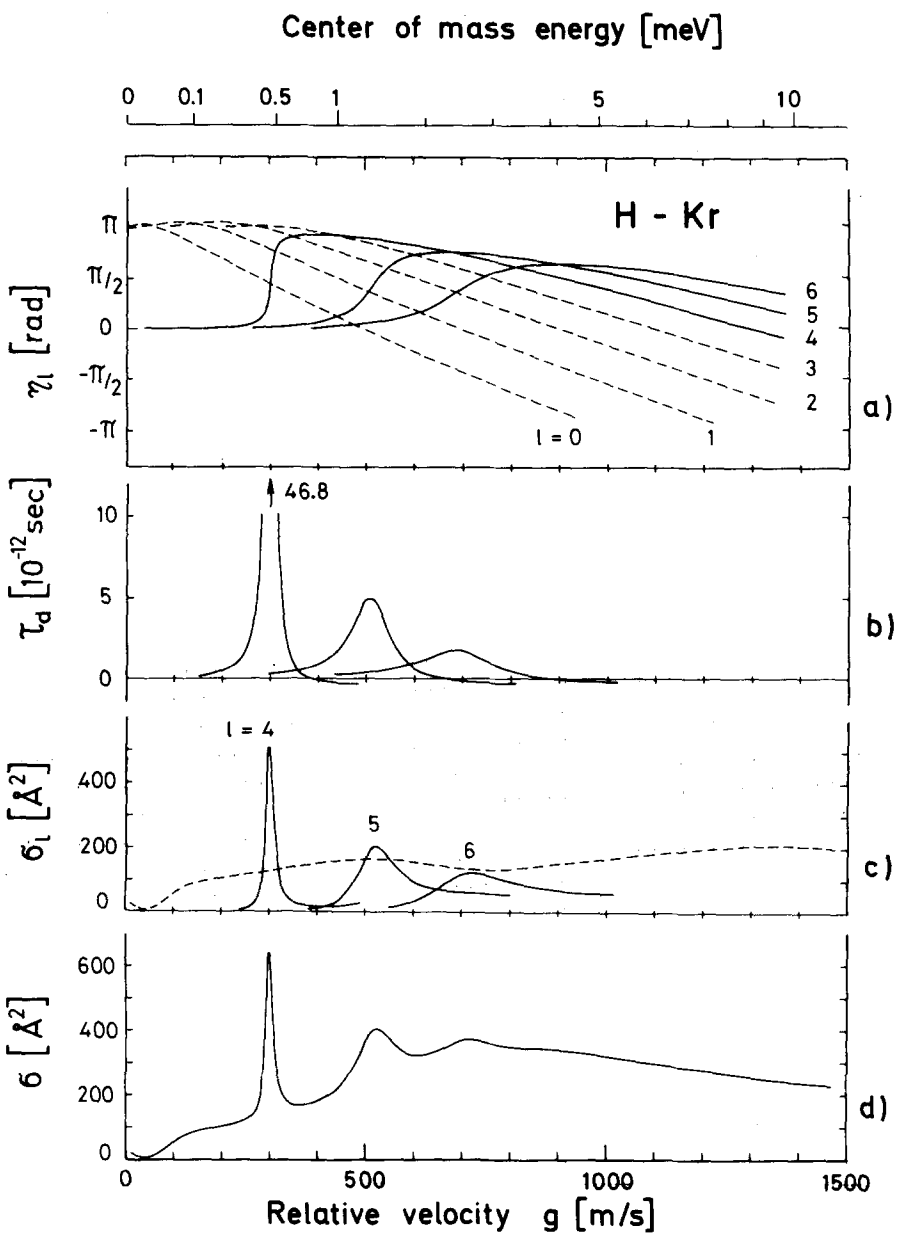

FIG. 3. The phase shifts for all the partial waves $l \leq 6$ are plotted for H–Kr as a function of the relative velocity in (a). The partial cross sections for $l = 4$, 5, and 6 as well as the sum of all partial cross sections but the resonant ones (dashed line) are shown in (c). The observable integral cross section is shown in (d). In (b) the time delay is plotted for the three resonances shown in (c). Note that as the phase shift shift passes through $\pi/2$ sharp resonance maxima and a large increase in the time delay occur. Since the phase is small at velocities below the resonance only maxima are observed for these systems.

mass spectrometer detector. Because of the large de Broglie wavelength (at $g = 300$ m/sec $\lambda_H = 13.3$ Å) the angular resolution of the detector is not critical and the usual cross section corrections[29] can be neglected. On the other hand scattering from the residual gas can be a problem[30] at the low laboratory velocities and for this reason the beam path in regions of moderate vacuum ($\simeq 10^{-6}$ Torr) was kept as short as possible. Since the hydrogen atom source, the converging beams target assembly and the detector are of unusual design and have not been described previously they are discussed in more detail below.

A. The hydrogen atom source

To obtain a cold but intense atom beam a standard discharge source originally developed for a source of a polarized protons[31] was modified by the addition of a moderator.[32,33] Figure 6 shows a detailed drawing of the H-atom source used in these experiments. H_2 is admitted into a water cooled Pyrex tube at a pressure between 0.3–0.5 Torr. Water cooling (~15 °C) not only serves to reduce the temperature of the gas in the discharge but also reduces the rate of recombination on the walls.[34] The degree of dissociation was found to be strongly affected by contamination of the walls and the discharge tube had to be cleaned by rinsing in concentrated hydrofluoric acid (40%–50%) after about 150–200 h. The discharge is powered by a 27.12 MHz welding generator (Type G 1200 56, Körting GmbH). The so called "Wendeltopf" resonator is essentially a $\lambda/4$ coaxial resonator.[35] The length of the inner conductor is reduced to about 15 cm by using a 5 turn helix. Power is coupled into the inner helix at a position which is determined by trial and error. One end of the helix is attached to the outer cylinder while the other end is free. The actual power dissipation was about 50 W. This type of resonator has several advantages: (1) The energy is concentrated on the axis and the stray high frequency fields are entirely suppressed by the copper tube sur-

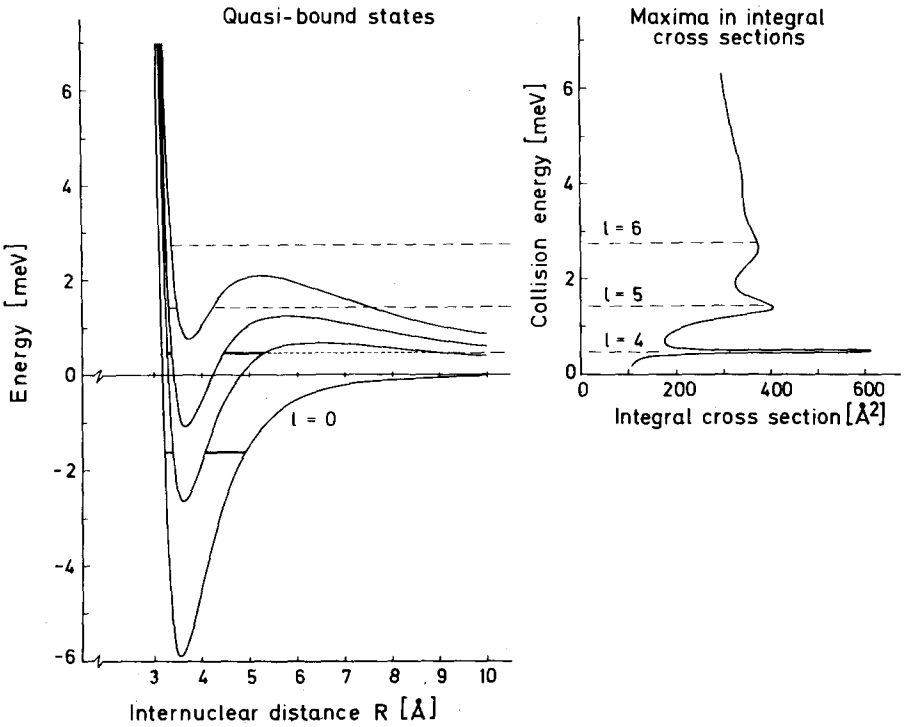

FIG. 4. The connection between the effective potential curves and quasibound state energy levels (on the left) and the expected quantum mechanical integral cross section (on the right) is shown for the example of a realistic LJ (12,6) potential for H–Kr.

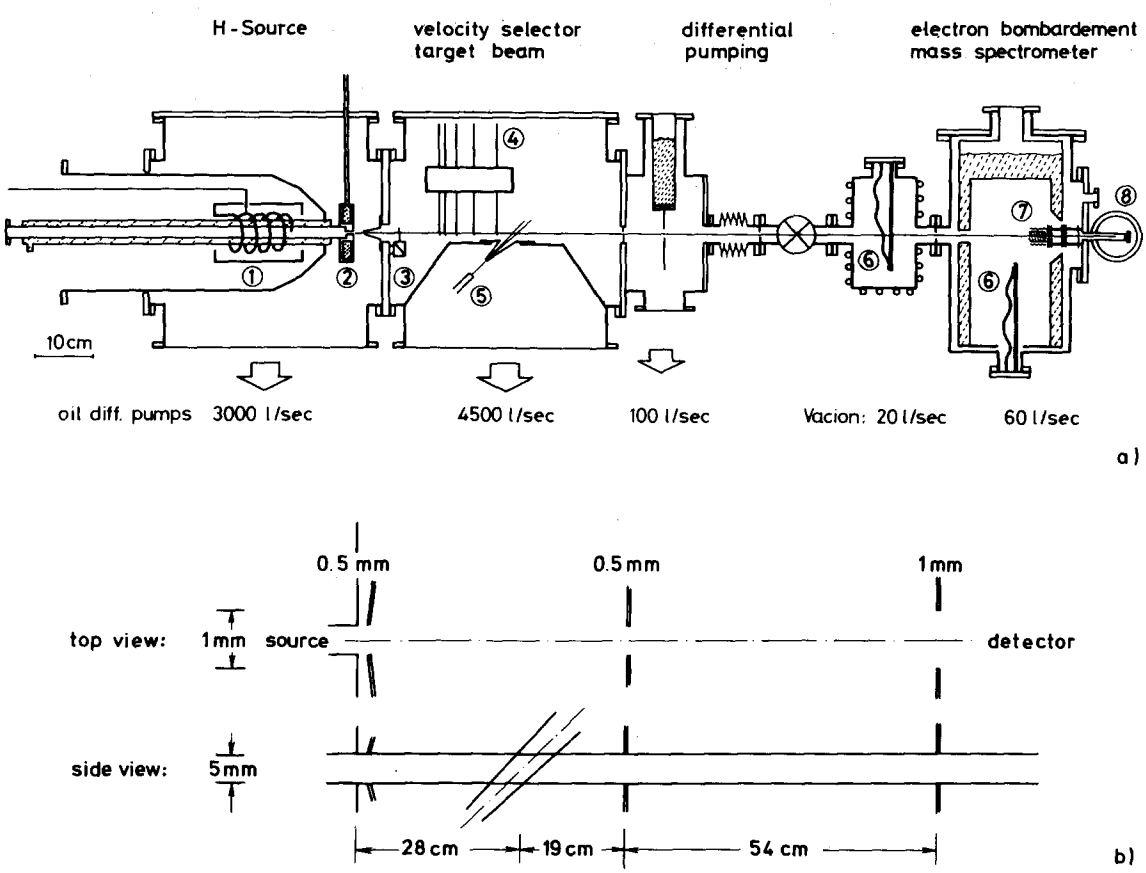

FIG. 5. The upper part (a) shows a roughly to scale schematic side view of the apparatus and its important components. The effective pumping speed is indicated below each chamber. The velocity selector chamber is evacuated by pumps (not shown) with a total effective speed of 2400 m/sec. The numbers refer to the following parts: 1, discharge resonator; 2, moderator; 3, beam flag; 4, velocity selector; 5, target nozzle beam; 6, titanium getter pump; 7, electron bombardment ionizer; 8, magnetic mass spectrometer and multiplier. In the lower part (b) the geometry of the beam slits is shown to a different transverse scale.

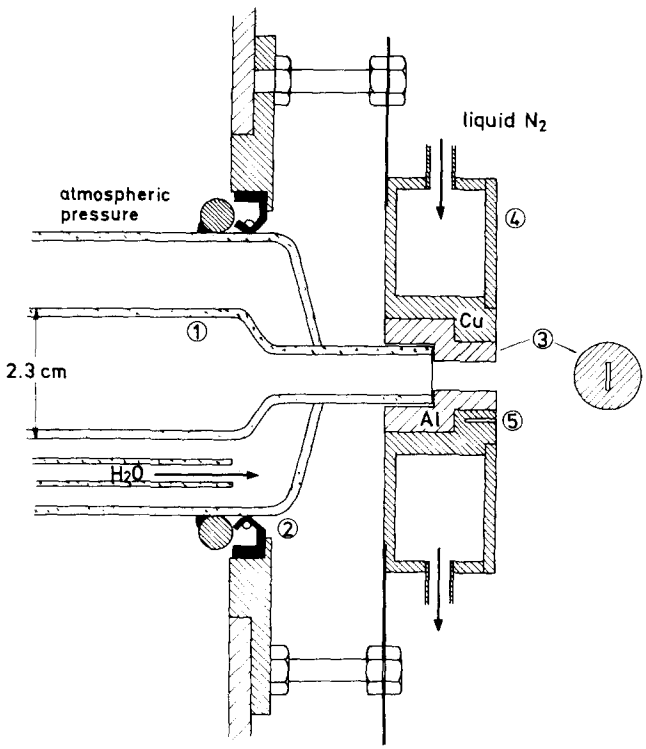

FIG. 6. Detailed view of the moderator. After leaving the glass discharge tube, 1, which is sealed to the supporting chamber by a spring loaded gasket, 2, the atoms and molecules pass through a 5 mm long aluminum channel, 3, with a rectangular cross section 0.5×5 mm. The channel is cooled by liquid N_2 passing through a copper cooling jacket, 4. The temperature is measured by a thermocouple, 5, in the jacket.

rounding the resonator as shown in Fig. 5(a). (2) The helical construction produces a strong axial ac magnetic field which extends well beyond the ends of the outer cylinder. Thus most of the molecules are dissociated along the axis in the center of the tube and extensive dissociation also occurs close to the exit slit which is about 8 cm to the right of the outer cylindrical wall of the resonator. (3) The construction is simple and the resonator shows good stability over long periods.

Details of the moderator construction can also be seen in Fig. 6. Essentially the moderator consists of a narrow rectangular channel in which the beam atoms undergo many wall collisions. In order to be effective the moderator surface should have a high accomodation coefficient. Moreover its thermal conductivity should be high in order to effectively pass on the heat of recombination to the cooling medium and prevent overheating of the surface. The ratio of accomodation to recombination coefficients determines the optimal dimensions for greatest cooling and least recombination. The following moderator materials were tried: Pyrex, boron nitride, copper, and aluminum. Of these aluminum had the best properties and beam temperatures of 90 °K and a high degree of dissociation was achieved. The optimal dimensions are given in the caption of Fig. 6. We attribute the good performance of aluminum to the formation of an oxide layer with chemical properties similar to Pyrex. Since the recombination coefficient of Pyrex shows a minimum at about 100 °K[34] we expect only little recombination at liquid N_2 temperatures. On the other hand aluminum has the big advantage over Pyrex of having a much greater thermal conductivity.

Figure 7 shows the measured velocity distribution of H atoms obtained with an aluminum moderator and compares it with the distribution expected for a source operating at 300 °K assuming the same total intensity. The source pressure was 0.4 Torr and the degree of dissociation in the beam as measured by the detector was typically 92%–95%. From a fit of the measured velocity distribution to a Maxwellian velocity distribution the effective source temperature was found to be 90 °K. The measured curve shows that the moderator provides a considerable gain in intensity at velocities below 2000 m/sec. At 300 m/sec the signal to background ratio is about unity and this is the lower limit at which measurements are feasible. Although higher source pressures lead to an increase in the total intensity the velocity distributions become narrower as a result of expansion cooling and the signal at the lowest velocities was consequently reduced.

B. The target nozzle beam

The target nozzle beam assembly was mounted directly beneath the primary beam. The nozzle (diameter = 0.06 mm) was mounted 10 mm below a sharply pointed conical skimmer (32°/25° full angle) of 25 mm length and opening of 0.6 mm diam. Because of the acute angle between the two beams the average distance between the nozzle orifice and the center of the primary beam was 61 mm; the target beam divergence as defined by the geometry[36] was 3.5°. The average angle of intersection was 46°. The entire nozzle skimmer unit could be moved in and out of the primary beam in a direction perpendicular to the primary beam. In this way the attenuation due only to the target beam could be measured since the additional attenuation produced by residual gas was the same in both positions of the target beam. The

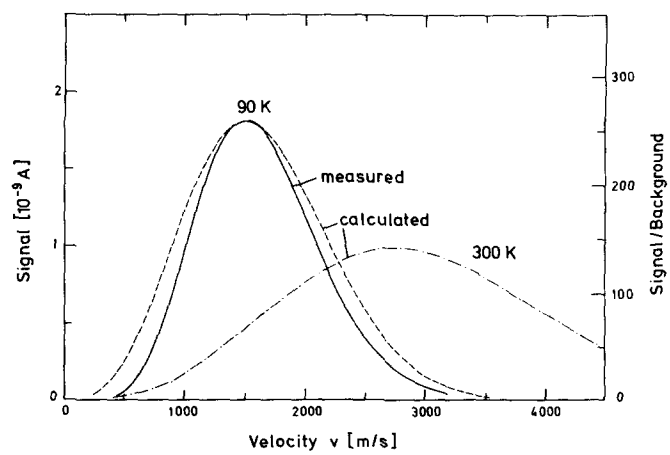

FIG. 7. Comparison of the measured distribution of H-atom velocities obtained with a liquid N_2 cooled moderator with the calculated Maxwell–Boltzmann distribution for the best fit temperature of 90 °C. At velocities below 2000 m/sec the cooling leads to a substantial increase in intensity over that expected for 300 °K.

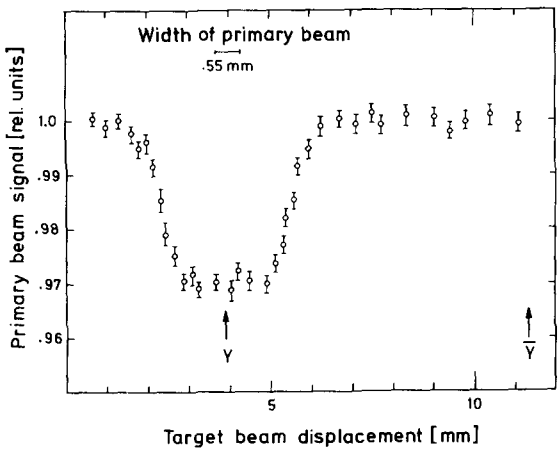

FIG. 8. The measured primary beam attenuation is plotted as a function of the displacement of the target nozzle beam perpendicular to the primary beam. To determine the attenuation due only to the target beam it was displaced between the position Y to the left, where the attenuation is largest, and the position $\bar{Y}$ where no attenuation due to the target nozzle beam is observed. Since the gas flow rate was unchanged the attenuation due to residual gas was the same in both positions.

optimal operating pressures, speed ratios, mean velocities and relative velocity half-widths (FWHM) were measured in another apparatus with nearly identical geometry.[37] The results are respectively: Ne: 3000 Torr, $S=26$, 790 m/sec, 6.5%; Ar: 1500 Torr, $S=26$, 558 m/sec, 6.5%; Kr: 990 Torr, $S=24$, 385 m/sec, 7.0%; Xe: 700 Torr, $S=19$, 308 m/sec, 8.6%. Figure 8 shows the measured attenuations of the primary beam as a function of the position of the target beam. The two positions actually used in the measurements are indicated. Depending on the system and relative velocity the attenuation varied between 1% and 5%.

C. The detector

The electron bombardment ionizer and mass spectrometer are similar to one described previously.[38] The ionizer had a measured sensitivity of 3×10^{-3} A/Torr for a Maxwellian H_2 beam (300 °K). The 5 cm radius permanent magnet mass spectrometer had a transmission of about 50% and a resolution of $\Delta m/m=8\%$ (FWHM). The relative amount of H_2 in the primary beam depends strongly on the selected velocity and for 90% degree of dissociation has a maximum of 30% at 600 m/sec and amounts to only 7% at 1500 m/sec. Since however only 1.5% of the H_2 intensity appears as a H^+ signal and the integral cross sections for H_2 and H are similar the correction for the H_2 component is always less than about 0.5%. Two differential pumping stages were provided between the scattering chamber and detector chamber. The stage closest to the detector was pumped by an ion sputter pump and a titanium getter pump and was designed in such a way that all rest gas molecules passing through it, had to undergo collisions on a titanium cooled surface.[39] As can be seen in Fig. 5 the ionizer was mounted inside a liquid nitrogen cold trap; the inner walls of which were covered by a titanium film. The pressure in the detector chamber was below the measuring limit of the gauge and the H_2 partial pressure was estimated to be less than 10^{-12} Torr.

The ions were counted and the signals were processed by a minicomputer (NOVA 1200, Data General), which also served for automatic control of the whole apparatus. The integral cross section was derived from successive measurements of the H^+ signal with the primary beam on and the target beam in alternate positions Y and $\bar{Y}$ (see Fig. 8) from which was subtracted the respective backgrounds measured with the primary beam turned off. Because of the small attenuation, small primary beam intensities and the relatively large background up to 3 h of measuring time were required to obtain a sufficiently small error in the integral cross section at one velocity setting.

D. Experimental errors

Of particular importance in an experiment of this type is the absolute determination of the relative velocity g since this determines the center of mass energy of the observed resonances. The absolute error in g is given by

$$dg=\left|\frac{\partial g}{\partial v}\right| dv+\left|\frac{\partial g}{\partial u}\right| du+\left|\frac{\partial g}{\partial \alpha}\right| d\alpha\ , \tag{11}$$

where dv, dv, and $d\alpha$ are the experimental uncertainties in the absolute velocities of both beams and the angle of intersection. The values of the coefficients are easily obtained by differentiation of Eq. (8). The result is that $\partial g/\partial v$ contributes most at large reduced velocities v/u; whereas $\partial g/\partial u$ contributes most at reduced velocities v/u smaller than 1. The last term contributes most at reduced velocities v/u in the vicinity of 1. The absolute accuracy of the primary beam velocity depends on the absolute calibration of the velocity selector. The velocity selector was calibrated by measuring the most probable velocity $\hat{v}$ of a He nozzle beam, which is known to be accurately given by

$$\hat{v}_{\mathrm{He}}=\sqrt{\frac{5kT}{m_{\mathrm{He}}}}\ . \tag{12}$$

The largest errors thus come from the temperature measurement. We estimate the overall absolute error in v to be about ±1%. The most probable velocities of the heavier rare gas target beams cannot be determined reliable in this way because of an unknown amount of condensation which may occur. For this reason we used the values reported in Sec. III B which agree with those from Eq. (12) to within 0.5%. We thus estimate that the errors in u are less than about ±1%. Probably the largest source of error in g comes from the uncertainty in the determination of α which is estimated to be ±1.0°. The resulting overall error in g is therefore about ±2% at large v/u. Other sources of systematic errors would affect the magnitude of the cross sections. Since the reproducibility of the absolute cross sections was found to be better than the statistical errors these errors can be neglected.

IV. EXPERIMENTAL RESULTS

All the measured cross sections presented in this section have been multiplied by a factor $v_0/\hat{g}$ and are

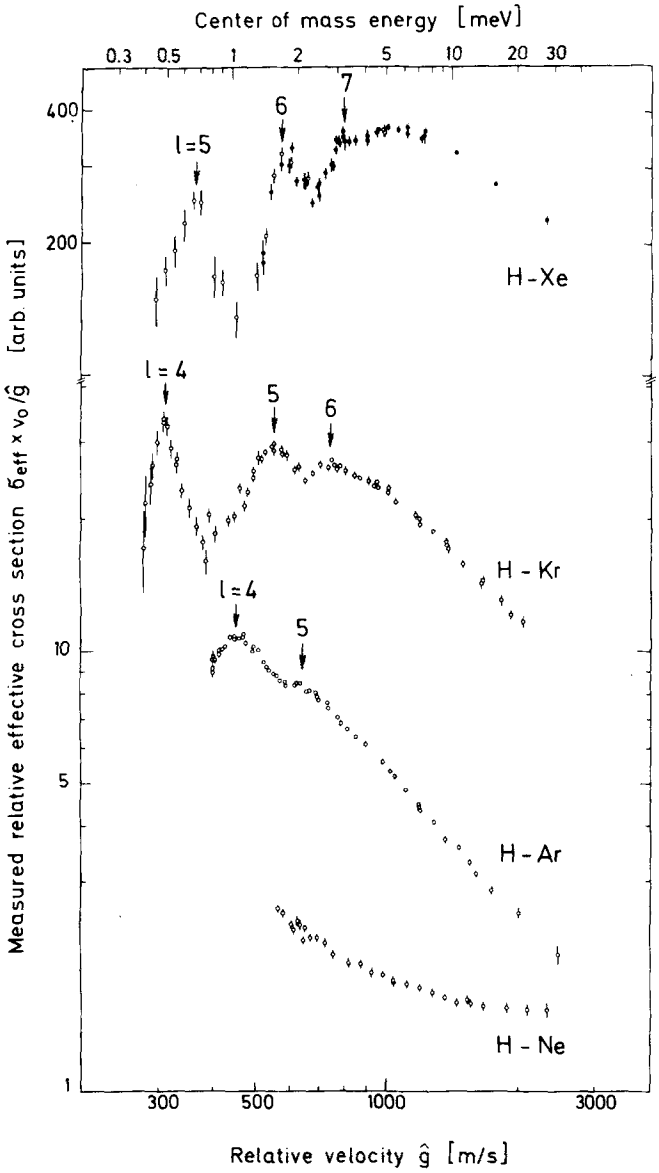

FIG. 9. The measured integral cross sections for the systems H–Ne, Ar, Kr, and Xe, multiplied by the factor $v_0/\hat{g}$, (v_0 is the primary beam velocity and $\hat{g}$ the most probable relative velocity), are plotted against the most probable relative velocity. The center of mass collision energy is indicated at the top abscissa. The arrows indicate the orbiting resonances and the indicated l-values are from a best fit of the data. The open circle data points were measured with an angle between primary and secondary beams of 46°. The solid points for H–Xe were measured with the two beams crossing at right angles. They have been shifted to match the other data points.

plotted as a function of $\hat{g}$, where $\hat{g}$ is calculated from Eq. (8). The cross sections corrected and plotted in this way take into account most of the kinematic corrections and in first approximation can be compared with theoretical predictions. To understand this we recall that the measured cross sections for a given primary beam velocity is averaged over the velocity distributions of the primary beam $P_1(v, v_0)$, the secondary beam $P_2(u)$, and the distribution over the angle of intersection $P_3(\alpha)$.

$$\sigma_{eff}(v_0) = \int_0^\infty \int_0^\infty \int_0^\pi \sigma(g)\, g/v\, P_1(v, v_0) P_2(u) P_3(\alpha)\, d\alpha\, du\, dv \,. \tag{13}$$

If the three distributions are compounded into a single distribution of relative velocities $P(g, v_0)$ for a given v_0 then the measured cross section is given approximately by[40]

$$\sigma_{eff}(v_0) \simeq \int_0^\infty \sigma(g)\, g/v_0\, P(g, v_0)\, dg \tag{14}$$

with[41,42]

$$P(g, v_0) = \int_v \int_u P_1(v, v_0) P_2(u)\, P_3(g, v, u) \frac{d\alpha}{dg}\, du\, dv \,, \tag{15}$$

where the variable α has been replaced with the aid of Eq. (8). The factor g/v_0 in Eq. (14) takes account of the different residence times of the primary beam particles in the scattering region. Because of their greater residence times slow particles have a greater *a priori* chance of being scattered than fast particles. Since the $P(g, v_0)$ function for our apparatus has a half width of only about 10% in g (see Sec. V B and Fig. 14) and is centered at g we can approximate Eq. (14) by

$$\sigma_{eff}(v_0) \simeq \hat{g}/v_0\, \sigma(\hat{g}) \,, \tag{16}$$

where $\hat{g}$ can be estimated in good approximation from Eq. (8). Note that g is only uniquely defined in terms of v_0 provided that v_0 is either always greater or smaller than $u\cos\alpha$. Here we deal only with $v_0 > u\cos\alpha$ since in the other case the correction g/v_0 becomes very large.

A. H-Ne, Ar, Kr, and Xe

Figure 9 shows the measured cross sections for these systems. The error bars in Fig. 9 are the standard deviations of the average value s_{av} ($= s/\sqrt{n}$, where s is the standard deviation of the single determinations and n the number of measurements). The actual data points, errors, and number of measurements have been deposited with Physics Auxiliary Publication Service.[43] Since the lowest relative velocity that can be achieved in the converging beams arrangement depends on u [see Eq. (9)] and since u in turn is inversely proportional to the square root of the target atom mass [Eq. (12)] the lowest relative velocities are achieved for the heaviest targets. This is clearly evident in Fig. 9 where the lowest velocity decreases in going from Ne to Ar to Kr. The lowest relative velocities achieved, 280 m/sec, correspond to an energy of 0.4 meV or about 5 °K!

As seen in Fig. 9 all of the systems except H–Ne show definitive evidence of several resonance maxima. The differences in the structure observed for the four systems follow the anticipated trend. The system with the heaviest target, H–Xe, which is expected to have the deepest potential well, shows four maxima as well as a broad glory maximum at about 1000 m/sec. H–Kr exhibits only three maxima and H–Ar only two. Finally H–Ne does not show any maxima in the velocity range explored. From the analysis of this data in terms of a potential as discussed in the next section it is possible to ascertain the value of l of the partial cross section

TABLE I. Measured velocities and energies of the observed resonances and assigned values of the orbital angular momentum quantum number.

System	Relative velocity g (m/sec)[a]	Center of mass energy (meV)	Assigned orbital angular momentum l
H–Ar	455 ± 10	1.05 ± 0.05	4
	660 ± 20	2.22 ± 0.12	5
H–Kr	312 ± 5	0.50 ± 0.02	4
	555 ± 10	1.59 ± 0.06	5
	755 ± 15	2.94 ± 0.12	6
H–Xe	362.5 ± 12	0.68 ± 0.04	5
	592 ± 20	1.80 ± 0.12	6
	790 ± 25	3.21 ± 0.20	7
	980 ± 25	4.94 ± 0.25	8
H_2–Ar	409 ± 7	1.66 ± 0.06	8
	520 ± 15	2.70 ± 0.15	9
	655 ± 20	4.25 ± 0.28	10
H_2–Kr	400^{+20}_{-15}	$1.63^{+0.16}_{-0.12}$	9
	512 ± 10	2.67 ± 0.10	10
	647 ± 15	4.27 ± 0.20	11
H_2–Xe	510 ± 30	2.65 ± 0.37	11

[a]Only the estimated errors in determining the peak location from the measured curves are indicated. The systematic errors in the absolute values which are of the order of ± 2% or less are not included.

contributing most to the observed resonances. These values are listed above the measured resonances in Fig. 9. The relative velocities, center of mass energies and assigned partial waves of the resonances are listed in Table I.

Figure 10 shows a panoramic view of the integral cross sections for H–Xe in which the new data of Fig. 9 is presented together with previously published data at higher velocities.[44] At high velocities the cross section goes over into the transition region and finally at the highest velocities the cross section approaches the region in which it is dominated by the repulsive potential. The best fit cross section at $g = 14 \times 10^3$ m/sec has a value of about 60 Å^2. This is roughly twice the classical value of R_0^2 (= 72 Å^2 for $R_0 = 3.4$ mm Å). The factor 2 is a quantum effect which arises from diffraction scattering.[45]

B. n-H_2-Ar, Kr, and Xe

These experiments were initially undertaken to explore the influence of the potential anisotropy on the orbiting resonances. Figure 11 shows the corrected measured cross sections as a function of the most probable relative velocity. The data points are also listed in Appendix A. The measurements were carried out with normal-H_2 (25% para-H_2 with even rotational quantum number j and 75% ortho-H_2 with odd j). In all of the measurements at $\hat{g} < 2000$ m/sec the moderator was used to lower the temperature of the beam so that nearly all the molecules were in their respective lowest states $j = 0$, and $j = 1$. The attenuation fluctuated between 1% and 6%. However because of the greater background on the H_2 mass (factor 20) the measurements took longer (up to a factor 2) than for H-atom scattering.

In all three systems resonance maxima were observed. Surprisingly the trend in the structure with increasing

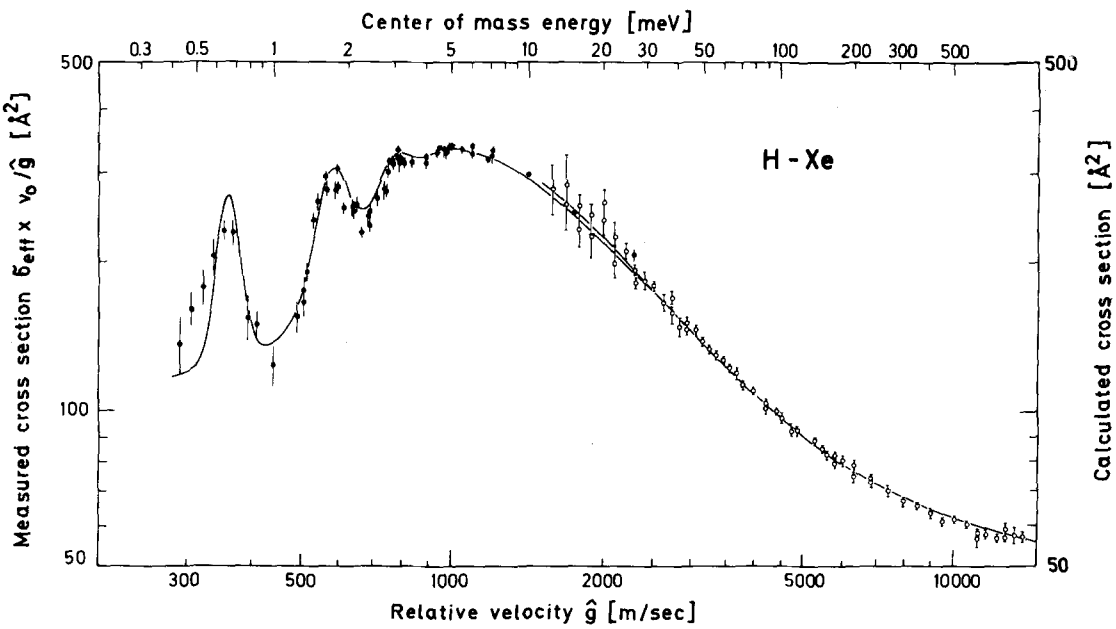

FIG. 10. The measured integral cross section for H–Xe multiplied by $v_0/\hat{g}$ (see caption Fig. 9) obtained in the present work (solid points) is compared with previously published data (open circles).[45] In the previous experiments the target beam was formed in a multichannel array. The cross section shows a single glory maximum at 1000 m/sec. With increasing velocity the cross section drops off as the long range attractive potential becomes less effective in deflecting particles. At the highest velocity the cross section (≃ 60 Å^2) is equal to roughly twice the geometric area of the repulsive core (πR_0^2) as expected because of diffraction scattering. Note that the experiments yield only relative cross sections. The absolute scale is determined from the calculation for the best fit potential.

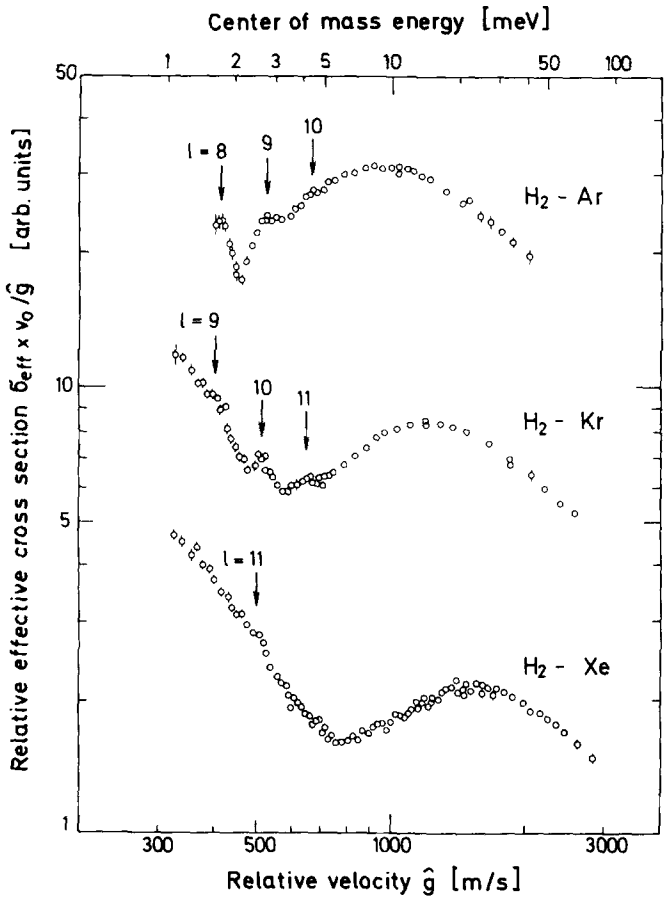

FIG. 11. The measured integral cross sections for the systems H_2–Ar, Kr, and Xe, multiplied by the factor $v_0/\hat{g}$, where v_0 is the primary beam velocity and $\hat{g}$ the most probable relative velocity. The arrows indicate the orbiting resonances and the indicated l values are from a best fit of the data.

mass of the rare gas atom seems reversed from that found with H atoms: H_2–Ar shows more structure than H_2–Xe. As discussed in the next subsection the potential anisotropy has no apparent effect on the H_2–Ar resonance so that this different behavior cannot be attributed to the anisotropy. The analysis in terms of an isotropic potential presented in the next section shows that the potentials are quite similar to the H-atom interactions and follow the same trends. Thus the explanation for the different behavior can only be due to subtle differences in the shape and the greater mass of H_2. The relative velocities, center of mass energies and assigned partial waves for these systems are also listed in Table I.

C. Comparison of integral cross sections for normal-H_2-Ar and para-H_2-Ar

To explore the possibility that the anisotropy of the potential was affecting the observed resonances the measurements on the system showing the most structure, H_2–Ar, were repeated with a para-H_2 beam. The H_2–Ar system was also chosen since its anisotropy has been measured and is about the same as for the other rare gases.[46] At 90 °K, 99% of the p-H_2 molecules is is expected to be in the $j=0$ quantum state which is spherically symmetric. Thus the scattering of molecules in this state depends only on the spherically symmetric part of the potential.[47] The techniques used to produce and analyze pure p-H_2 are the same as those used in another experiment and will be described in a forthcoming paper.[48]

Figure 12 shows the comparison of the two sets of measurements. No differences can be observed within the experimental limits. This result indicates that the anisotropy has no measurable effect on the cross sections for the H_2–rare gas systems in the velocity range of these experiments. The threshold for rotational excitation $j=0\rightarrow 2$ is also shown in this figure. Since the energies are below the threshold this process can be neglected in the data analysis.[47]

V. DETERMINATION OF INTERMOLECULAR POTENTIALS

A. Potential region probed

Initially two different inversion schemes were tried in order to obtain model independent potential parameters from the resonance location and widths. The one scheme is related to the standard procedure in infrared spectroscopy in which the spacing of the rotational levels serves to determine the expectation value of the internuclear distance R_m and the vibrational level for zero rotational quantum number the well depth ϵ.[49] This procedure is practicable and yields results of moderate accuracy. The analysis and the results will be reported in a subsequent paper.[50] The other inversion procedure is based on a semiclassical method initially proposed by Stwalley[28] and is similar to methods discussed by Bernstein and others.[18] This method is based on the assumption that the energies E_{LBM} of the "Locus of Barrier Maxima" can be established from the observed resonance energies. If this is the case and if the orbital angular momentum quantum number is known the po-

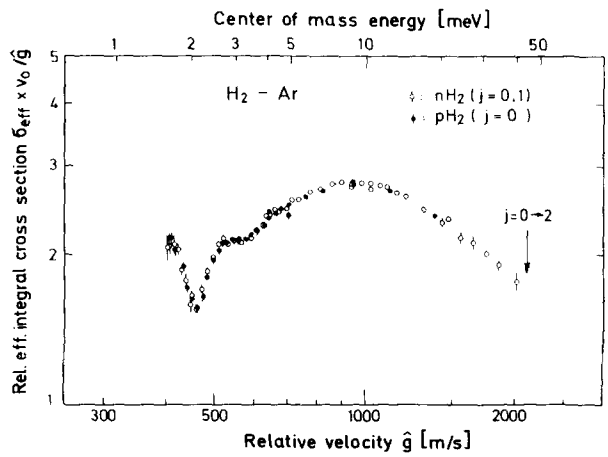

FIG. 12. The H_2–Ar integral cross sections, multiplied by $v_0/\hat{g}$, measured with n-H_2 (open circles) are compared with measurements with pure p-H_2 (full circles) in which all the molecules are in the lowest $j=0$ rotational state. In this state only the spherical symmetric part of the potential is probed. The negligible differences in the two sets of results rules out any appreciable effect of the anisotropy on these measurements. The arrow at the right shows the threshold for rotational excitation.

tential at the positions R_{max} for various l can be determined:

$$E_{LBM} = V_{eff}(l, R_{max,l}) \tag{17}$$

$$= V_0(R_{max,l}) + \frac{\hbar^2 l(l+1)}{2\mu R^2_{max,l}} \ . \tag{18}$$

It remains to determine $R_{max,l}$. Differentiation of Eq. (18) yields

$$\frac{dE_{LBM}}{dl(l+1)} = \frac{\hbar^2}{2\mu R^2_{max,l}} \ . \tag{19}$$

Thus $R_{max,l}$ can be obtained from the slope of the curve of E_{LBM} vs $l(l+1)$ at the corresponding values of l. From this analysis we see that the resonance energies provide information mostly on the long range part of the potential in the vicinity of $R_{max,l}$. This inversion method was tried on H–Xe but did not prove to be sufficiently precise to be useful. The main difficulty was the accurate estimation of the corrections needed to obtain E_{LBM} from the observed resonance energies.[51] This is related to the fact that the vibrational level spacings in these weakly bound light systems are too widely spaced to apply semiclassical methods.

To explore further the potential range probed in these experiments a quantum mechanical approach based on the Calogero variable phase method[52] used in earlier studies was applied to this problem. In the Calogero method the scattering phase is calculated from $R=0$ out to some point R'. Thus it is possible to calculate the partial integral cross section as a function of R' by inserting the phase for R' into Eq. (4). The asymptotic cross section for $R \to \infty$ thus corresponds to the observable cross section. Figure 13(a) shows the partial cross section calculated for H–Kr as a function of R for the energies of the $l=4$, 5, and 6 resonances. From these results we see that the major part of the cross section accrues in a narrow range of R values centered about the maximum of the corresponding part of the effective potentials shown in Fig. 13(b). The ranges drawn in the bottom part of Fig. 13(b) span the R range contributing 95% to the asymptotic cross section. These quantum results confirm the predictions of the previously discussed semiclassical inversion theory that the R range contributing most to the cross section is in the vicinity of $R_{max,l}$.

The foregoing analysis covers only one aspect of the inversion problem, namely the potential region contributing to the *magnitude* of the cross section at resonance. Obviously, as indicated by the spectroscopic analysis, the potential well depth and location also determine energetic *locations* of the resonances. Thus the question of the regions probed by the entire velocity dependence of the integral cross section is a complicated issue and only partly answered by curves such as Fig. 13. In view of this and the difficulties experienced with the inversion procedures we used the customary trial and error procedure to obtain a best fit of the cross section data. In the course of this work it was found that the cross sections were extremely sensitive to the exact shape of the potential and in order to speed up the convergence it was necessary to take into account all the available theoretical and experimental information on the potentials in the analysis. Nevertheless because of the sensitivity it was difficult in a number of cases to converge on an entirely satisfactory fit of the data. This leads us to believe that the best fit potentials for all systems with the exception of H–Ne and possibly H–Ar are nearly unique and quite close to the true potentials. Moreover the data provide a very critical test of a given potential model.

B. Corrections to the theoretical cross section

As discussed in Sec. III a correction for the insufficient angular resolving power is not required at the low velocities of these measurements. The velocity smearing is however important since it tends to wash out and broaden the resonance maxima. For this reason all the comparisons reported in this section were made using the approximation of Eq. (14) and not the further going approximation Eq. (16). As with the measurements the factor g/v_0 was corrected for by multiplying the calculated cross sections by $v_0/\hat{g}$. To calculate the relative velocity smearing function $P(g, v_0)$ the following approximations were used: (1) The primary velocity distribution $P_1(v, v_0)$ was assumed to be triangular with a half-width $\Delta v/v$ of 6%. (2) The target beam velocity distribution $P_2(u)$ was assumed to be Gaussian with the half-widths given in Sec. III B. (3) The angular distribution $P_3(\alpha)$ of the target beam was assumed to be rectangular. (See Fig. 8.) With these approximations $P(g, v_0)$ was calculated from Eq. (15). Figure 14 shows calculated distributions $P(g, v_0)$ for a range of values of v_0/u for $\alpha = 46°$, $u = 400$ m/sec. $\Delta v/v = \Delta u/u = 6\%$ (FWHM) and $\Delta\alpha = 3.5°$ (FWHM). These distributions are expected to be nearly independent of u and correspond closely to the conditions of these experiments. Since the distributions at small v_0/u, in the region of greatest interest, are nearly Gaussian they were approximated in the integration of Eq. (14) by a Gaussian distribution with the same half-width. Theoretical cross sections calculated in this way were checked against calculations based on the exact expression, Eq. (13) and found to agree within better than 0.2%. In subsequent tests of potential models the distributions of Fig. 14 should be used in comparing potential models with the data reported on here. Since Eq. (16) takes account of the major influence of smearing and the $P(g, v_0)$ functions are centered on g (see Fig. 14) only the half-widths and resonant heights are noticeably changed by the use of Eq. (14).

C. Potentials for H-Ne, Ar, Kr, and Xe

The potentials for these systems have been extensively studied in the past. H being a free radical spectroscopic and bulk experiments are difficult to perform and no quantitative information is available from these sources. The first experimental determinations by Bickes *et al.*[44] were based on integral cross section measurements at high velocities in the range between 1.4 and 14×10^5 cm/sec ($0.01 \leq E_{c.m.} \leq 1.00$ eV). The results could be fully explained in terms of the simple two parameter Lennard-Jones (12, 6) and the three

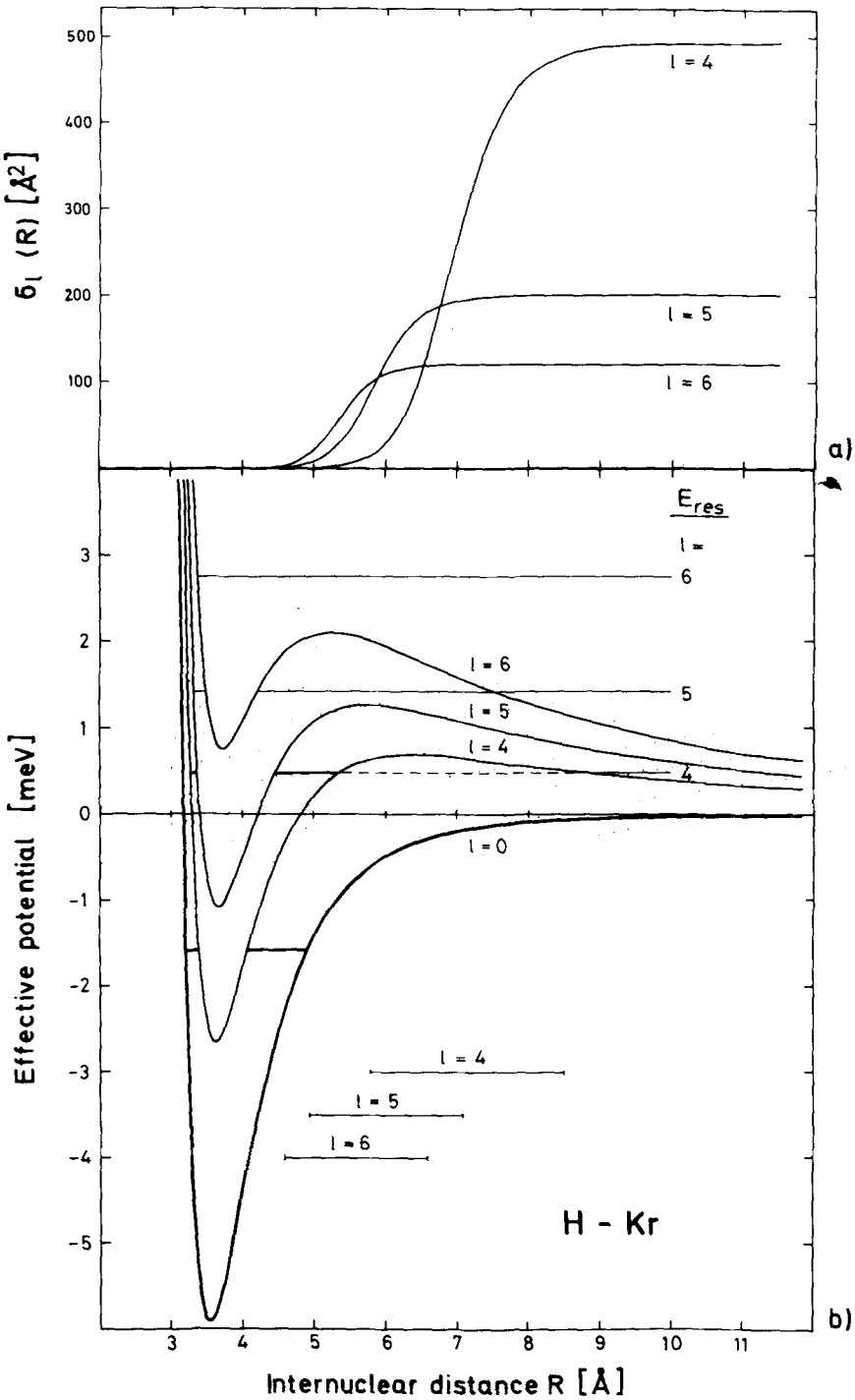

FIG. 13. The region of the potential probed by the partial cross section at resonance has been examined by the Calogero variable phase method. In (a) the partial cross sections of the $l = 4$, 5, and 6 resonances at the energies shown in (b) are shown as a function of R. The ranges contributing 95% to the cross section are shown as horizontal bars in (b). The analysis confirms the predictions of the semiclassical inversion theory that the region in the vicinity of the maxima of the effective potentials contributes most to the cross section.

parameter Slater–Buckingham exp(α, 6) potential models. More recently differential cross sections have been reported for H–Ar by Bassi *et al.*[53] Because of the simplicity of the H atom these systems have also attracted some theoretical attention. Wahl and coworkers have carried out extensive *ab initio* calculations using MCSCF techniques for H–Ne, Ar, and a pseudopotential variant of the MCSCF method for H–Kr and Xe.[54] Another important source of data are the calculated values of the long range dispersion constant C_6, C_8, and C_{10} reported by Stwalley.[55] Previous experimental and theoretical potentials and our best fit potentials are discussed in turn for each of the four systems next.

1. H–Ne

Neither resonance nor glory structures could be observed for this system so that the determination of a unique potential is not to be expected. The measurements were undertaken in order to clear up the large discrepancy between the earlier potential of Bickes *et al.*[44] and an *ab initio* potential calculated by Wahl and co-workers.[54] Table II describes the earlier experimental potential

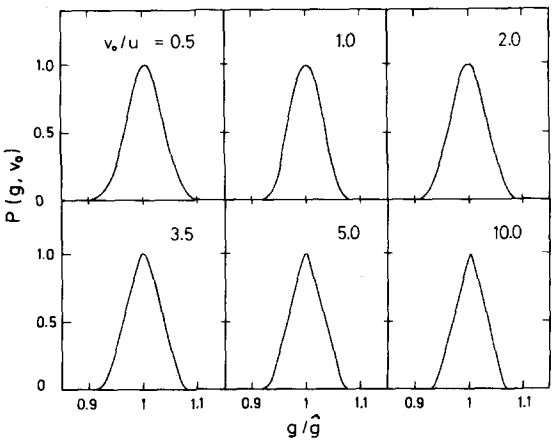

FIG. 14. Normalized calculated distributions $P(g,v_0)$ are plotted as a function of the relative velocity for a range of values v_0/u. The calculations are for $\alpha = 46°$, $u = 400$ m/sec with $\Delta v/v_0 = \Delta u/u = 6\%$ (FWHM) and $\Delta\alpha = 3.5°$. The distributions are nearly independent of u.

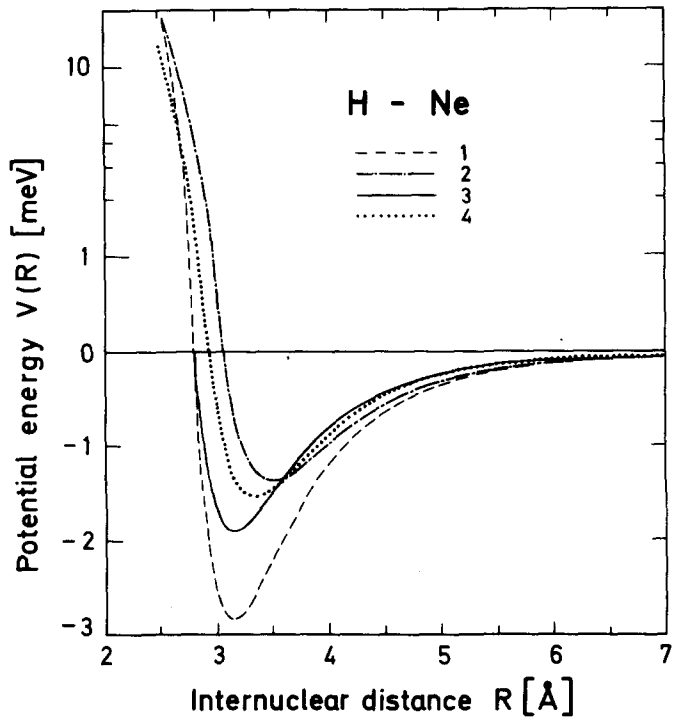

FIG. 15. Experimental and theoretical potentials for H–Ne are plotted as a function of the internuclear distance. The potentials 2 and 4 are from MCSCF calculations and 1 is from a previous beam experiment at higher velocities. Potential 3 is a potential, which provides a best fit of the present low velocity data. For details on these potentials see Table II.

designated by 1, an earlier theoretical potential, designated by 2 and a more recent refined theoretical potential, 4. The potential 3 refers to the best fit potential obtained in the course of this work. The large discrepancy between the earlier experimental and the theoretical potentials is clearly apparent in Fig. 15 which shows all the potentials listed in Table II. Figure 16 presents a comparison between calculated cross sections for four of these potentials and the measured data. In addition to these new measurements we also show the only available absolute cross section ($\sigma = 40.8$ Å$^2 \pm 5\%$) at 5000 m/sec.[44] This value was actually extrapolated from an earlier measurement,[56] carried out at 8125 m/sec, by a calculation based on potential 1. The estimated error

TABLE II. Potential models for H–Ne.

Designation	Model	Parameters[a]	Source	Reference
1	LJ (12,6) and exp(α,6)	$\epsilon = 2.82\ (\pm 0.10)$[b] $R_m = 3.15\ (\pm 0.15)$	integral cross sections measured at $v > 1.8\times10^3$ m/sec	Bickes *et al.*[45]
2	exp(α,6)	$\epsilon = 1.35$ $R_m = 3.50$ $\alpha = 12$	slightly modified from an early MSCSF calculation	Das, Wagner, and Wahl[54a]
3	2×LJ (12,6)	$\epsilon = 2.82$, $R_0 = 2.806$ for $R < R_0$ $\epsilon = 1.90$, $R_m = 3.15$ for $R \geq R_0$	best fit	present
4	WDW1[c]: $V(R) = (a+bR+cR^2)\exp(-\alpha R)$ $-\frac{d}{R^6} - \frac{f}{R^8} - g\,e^{-\beta R}$ $R \geq R_1$ $= h\,e^{-\gamma R} - \epsilon$ $R \geq R_1$	$a = 116\,121$ $b = -45\,709.4$ $c = 4\,664.74$ $\alpha = 2.664\,51$ $d = 3229.28$ $f = 8\,976.65$ $g = 8\,975.87$ $\beta = 2.815\,69$ $h = 2\,533\,610$ $\gamma = 4.821\,12$ $\epsilon = 1.5312$ $R_m = 3.33$ $R = 2.646$	most recent MCSCF calculation	Das, Wagner, and Wahl[54b]

[a]All parameters are in units of meV and Å.
[b]The errors are those listed in Ref. 44 and span the range resulting from data evaluation using both the LJ(12,6) and the Buckingham–Slater exp(α,6) potentials. Only the indicated values were used in the calculations.
[c]This potential model was proposed by Wagner, Das, and Wahl.[57]

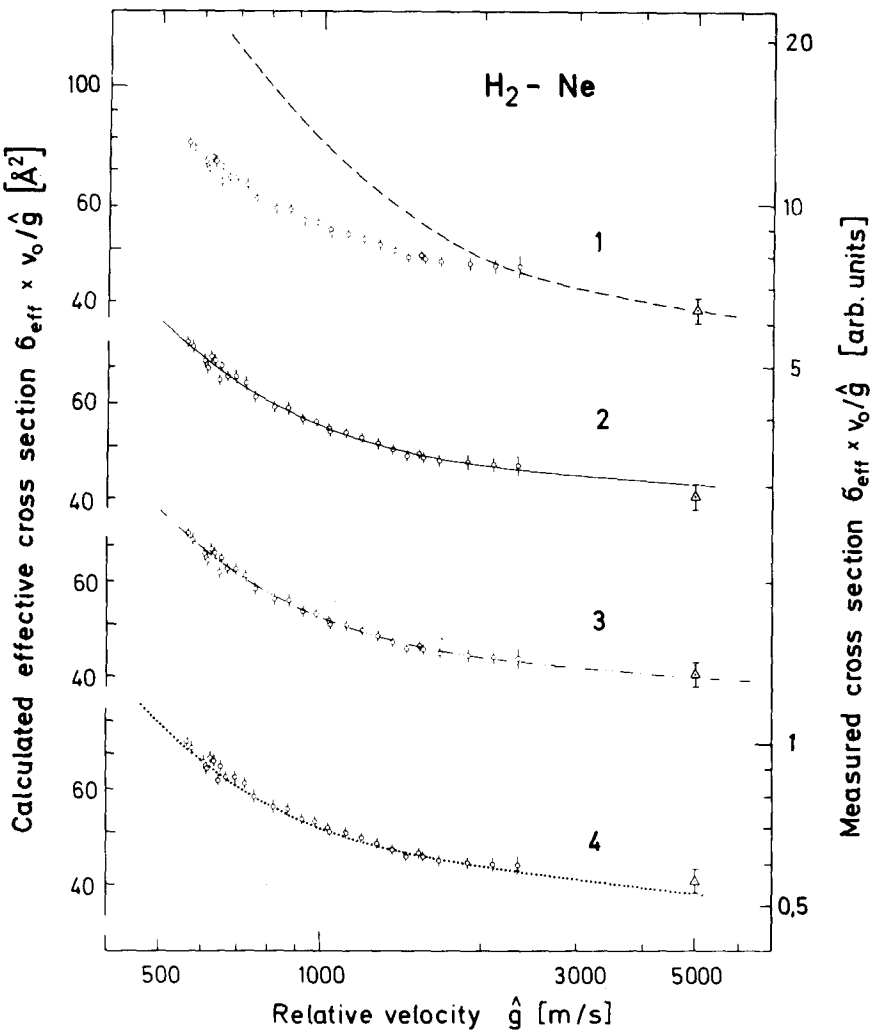

FIG. 16. The velocity dependence of cross sections calculated (left ordinate) for various potential models for H–Ne are each compared with the present measurements of relative cross sections (right ordinate). The potential models are described in Table II and plotted in Fig. 15. The absolute cross section shown at 5000 m/sec (⧖) is taken from Bickes *et al.*[45] The other experimental cross sections were shifted slightly in the vertical direction in order to provide a best fit. The apparatus smearing was accounted for in the calculations as discussed in Sec. V B.

also includes a possibly small error incurred in the extrapolation. In comparing the calculated absolute cross sections with the calibrated measurements these were shifted slightly in the vertical direction to provide the best possible fit. From Fig. 16 we conclude that the new measurements definitely rule out the deep well of the earlier experimental potential 1. Both theoretical potentials 2 and 4 and the best fit potential 3 provide a reasonably good fit of the data. Potential 3 differs only in that because of its smaller value of R_0 it provides a better fit of the absolute cross section at 5000 m/sec. The broad range spanned by the potentials 2, 3, and 4 as shown in Fig. 15 indicates the insensitivity of the measured cross sections in this particular system.

Finally we note that the failure of the earlier experimental potential 1 in fitting the low velocity data is not entirely unexpected. As pointed out in the original paper[44] a Calogero variable phase analysis of the data shows that a range of potentials with well depths between about 2 and 4.5 meV and R_0 in the range 2.65–2.90 Å is expected to include the true potentials with a confidence of 70%. In fact the high velocity data provides a precise model independent determination of the repulsive potential at only one point, 2.55 Å where the potential is about 15 meV. Whereas the potentials 1 and 2 agree with experiments in this regard, the new theoretical potential 4 is too small in the repulsive region. In the attractive region however the potential 4 is an improvement over the earlier theoretical potential 2, since it has the smaller value of R_0 and is closest to the range of R_0 values consistent with the earlier measurements.

2. H–Ar

This system has received more attention than all the other H-atom systems. Because of the larger well depth the integral cross section measurements of Bickes *et al.*[44] are quite sensitive to the well region. Moreover since an absolute cross section was available[56] it was possible to determine both ϵ and R_m (potential 1) with reasonable accuracy. The absolute value of the cross section measured at high velocities was not used in the present analysis for the following reason. In this case the uncertainties in extrapolating down to low velocities were considered to be too large since the extrapolation depends more sensitively on the assumed potential model than in H–Ne. More recently Bassi *et al.*[53] have measured diffraction oscillations in small angle differential cross sections at $E_{c.m.} = 67.4$ meV. These measurements are very sensitive to the absolute value of R_0 and rather insensitive to ϵ especially in view of the large collision energy which is a factor 15 greater

TABLE III. Potential models for H–Ar.

Designation	Model	Parameters[a]	Source	Reference	Goodness of fit: χ^2 [b]
1	LJ(12,6) and exp(α,6)	$\epsilon = 4.73\ (^{+0.22}_{-0.15})$[c] $R_m = 3.54\ (\pm 0.13)$	integral cross sections measured at $v > 1.6$ 10^3 m/sec	Bickes *et al.*[44]	1870
2	W D W 1[d]	$a = 63\,350\,000$ $b = -51\,310\,000$ $c = 11\,880\,000$ $\alpha = 4.384$ $d = 8269$ $f = 73\,190$ $g = 800.9$ $\beta = 1.62$ $h = 13\,890\,000$ $\gamma = 4.817$ $\epsilon = 4.156$ $R_m = 3.571$ $R_l = 2.19$	MCSCF calculation	Wagner *et al.*[57]	270
3	W D W 1	Same as 2 but the R axis has been expanded by 1.4% $\epsilon = 4.16$ $R_m = 3.62$ $R_0 = 3.15$	differential cross section measurements at $E_{c.m.} = 67.4$ meV and present best fit	Bassi *et al.*[53]	165
4	W D W 1	$a = 63\,349\,400$ $b = -51\,305\,200$ $c = 11\,876\,500$ $\alpha = 4.381\,46$ $d = 12\,342.6$ $f = -53\,649.1$ $g = 14747.1$ $\beta = 2.192\,08$ $h = 84\,566\,600$ $\gamma = 5.417\,36$ $\epsilon = 4.8545$ $R_m = 3.49$ $R_l = 2.19$	improved MCSCF calculation	Das *et al.*[54b]	1932

[a] All parameters are in units of meV and Å.

[b] χ^2 is defined by

$$\chi^2 = \sum_i \left[\frac{\sigma_{\text{eff}}^{(i)}(v_0) - f\,\sigma_{\text{expt}}^{(i)}(v_0)}{f\,\Delta\sigma_{\text{expt}}^{(i)}} \right]^2 ,$$

where $\sigma_{\text{eff}}^{(i)}$ is the calculated cross section at velocity point i, $\sigma_{\text{expt}}^{(i)}$ is the average experimental cross section. f is a constant factor for shifting the relative cross sections to provide a best fit of the absolute theoretical values and $\Delta\sigma_{\text{expt}}^{(i)}$ is the standard deviation of the average value.

[c] See footnote b of Table II.

[d] See Table II for the analytic expression.

than the well depth. A best fit to these differential cross sections was provided by a slight modification of an early MCSCF theoretical potential (potential 2) calculated by Wagner *et al.*[57] to yield potential 3. Very recently Das *et al.*[54b] have reported a refined MCSCF potential (potential 4). The potentials 1–4 are summarized in Table III, where, in addition to the potential parameters, the χ^2 values, obtained from a comparison of the calculated with measured cross sections, are also listed. These values are included as a guide for judging a given potential; however, they should not be overinterpreted since small shifts in the energetic location in a resonance can lead to relatively large contributions to χ^2. Figure 17 compares the shapes of all four potentials. There we see that the potentials 2 and 3 lie quite close to each other. Surprisingly the latest theoretical potential 4, however, lies closest to the early experimental potential 1. Figure 18 shows comparisons between calculated and experimental cross sections for all the potentials. There we see that 3 provides a best fit of the data. The theoretical potentials 2 and 4 however also predict cross sections close to the experimental ones. Potential 2 fails in predicting the maximum at 450 m/sec and potential 4 overemphasizes the weak glory maximum at 1000 m/sec. The sensitivity of the data is better than in H–Ne, but a more stringent test of these potentials would be provided by the observation of the $l = 3$ resonance which is expected near g

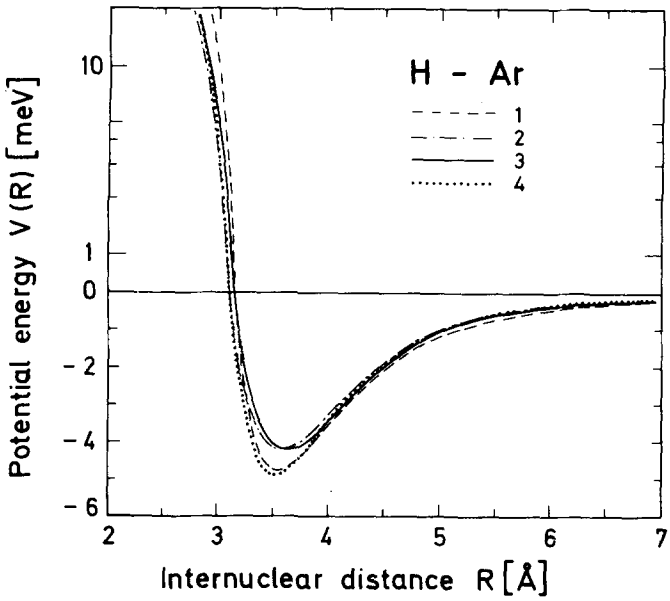

FIG. 17. Experimental and theoretical potentials for H–Ar are plotted as a function of the internuclear distance. The potentials 1 and 3 are from previous beam experiments. The potentials 2 and 4 are from MCSCF calculations. Potential 3 provides a best fit of the present experiments. For details on these potentials see Table III.

$\simeq$230 m/sec or by measurements of the system D–Ar.

3. H–Kr

Less is known about the heavier systems H–Kr and H–Xe. Here several orbiting maxima were seen and the measurements contain much more information on the potential. Unfortunately the customary *ab initio* methods are much more difficult. Nevertheless Das *et al.* [54b] have recently reported an *ab initio* calculation based on a pseudopotential variant of the MCSCF method. This potential designated by 3 is compared with the only previous experimental potential 1 and the potential 2 providing a best fit of our data in Table IV and Fig. 19. Figure 20 compares the calculated cross sections for all three potentials with the experimental cross section. It is seen that both potentials 1 and 3 can be definitely ruled out by the data. Potential 1 was obtained from measurements of integral cross sections at high velocities[44] similar to the data used in obtaining the potentials 1 for H–Ne and H–Ar, only in this case they are more sensitive to the well parameters. Unfortunately however an absolute value was not available and thus the data only provide information on the product ϵR_m. ϵ and R_m were estimated with the aid of combining rules. Thus the small error in the shape is understandable. The product ϵR_m of potential 1 agrees with that of the best fit potential within 4%.

After experience indicated that a satisfactory fit was not possible using the simpler 3 parameter Lennard-Jones or Slater–Buckingham models the potential model 2 consisting of a LJ (12, 6) potential at short and intermediate distances and a three term dispersion expansion at long distances was used. This is probably the simplest model which provides a sufficiently realistic description of the long range behavior. Similar potential models have been used with good success in predicting and fitting experimental data. [58] In this case the C_6 coefficient was taken from calculations by Starkschall, [59] while C_8 and C_{10} were taken from a recent estimate reported by Stwalley. [60]

4. H–Xe

Here the overall situation is similar to that for H–Kr. As with H–Kr the only previous experimental determination[44] is sensitive to the product ϵR_m and an approximate procedure also had to be used to extract values for ϵ and R_m. No other experimental determinations of the potential in the well region are known to us. The new pseudopotential variant of the MCSCF method was applied to this system as well. [54b] Table V summarizes the important parameters of the three potential models. The parameters of potential 1 have been slightly modified from the originally reported determination to provide a best possible fit of the data within the framework of the simple LJ (12, 6) model. The model potential 2 is the same as that used successfully to fit the H–Kr data. It provides a more realistic description of the long range behavior since it contains a three term dispersion expansion. The C_6, C_8, and C_{10} parameters were also taken from Refs. 59 and 60. As seen in Fig. 21 this potential has a significantly different long range shape than the LJ (12, 6) potential. After optimizing the well parameters ϵ and R_m this potential provides a somewhat better fit than the simple LJ (12, 6) potential. Although the reduction in χ^2 is not spectacular (see Table V) examination of Fig. 22 also shows that potential 2 fits the data better in the region of the resonance at 550 m/sec. The use of the more realistic potential model 2 leads to a significant change in ϵ from 6.65 to 7.08 meV. Finally we note that the *ab initio* potential lies very close to the best fit potential (see Fig. 21) even though the large discrepancy between experimental and theoretical cross sections suggests much larger differences in the potentials. This result and the trend observed in going from H–Ar to Xe shows how the availability of an increasing number of resonance maxima greatly increases the sensitivity of the experiment to very small differences ($\approx$1%) in the potentials.

Examination of Fig. 22 shows velocity regions in which there is still a small discrepancy between the best fit cross sections and the measured values. Especially at low velocities between 300 and 350 m/sec the measured peak appears broader than the calculated one. This discrepancy is not fully understood and could not be removed by further optimization of the potential parameters. Possibly it is due to errors in the simulation of the velocity smearing or to the influence of a small amount of Xe dimers. Of all the rare gases Xe is most likely to show dimer formation in nozzle beams and the presence of small concentrations cannot be ruled out.

H–Xe is the only rare gas hydride which may have two vibrational states. The value of B ($=2\mu\epsilon R_m^2/\hbar^2$) for the best fit LJ (12, 6) potential is 47.5 ($\pm$3%) and is within the errors equal to the critical value of 46.6[61] indicating that a second bound state is possible.

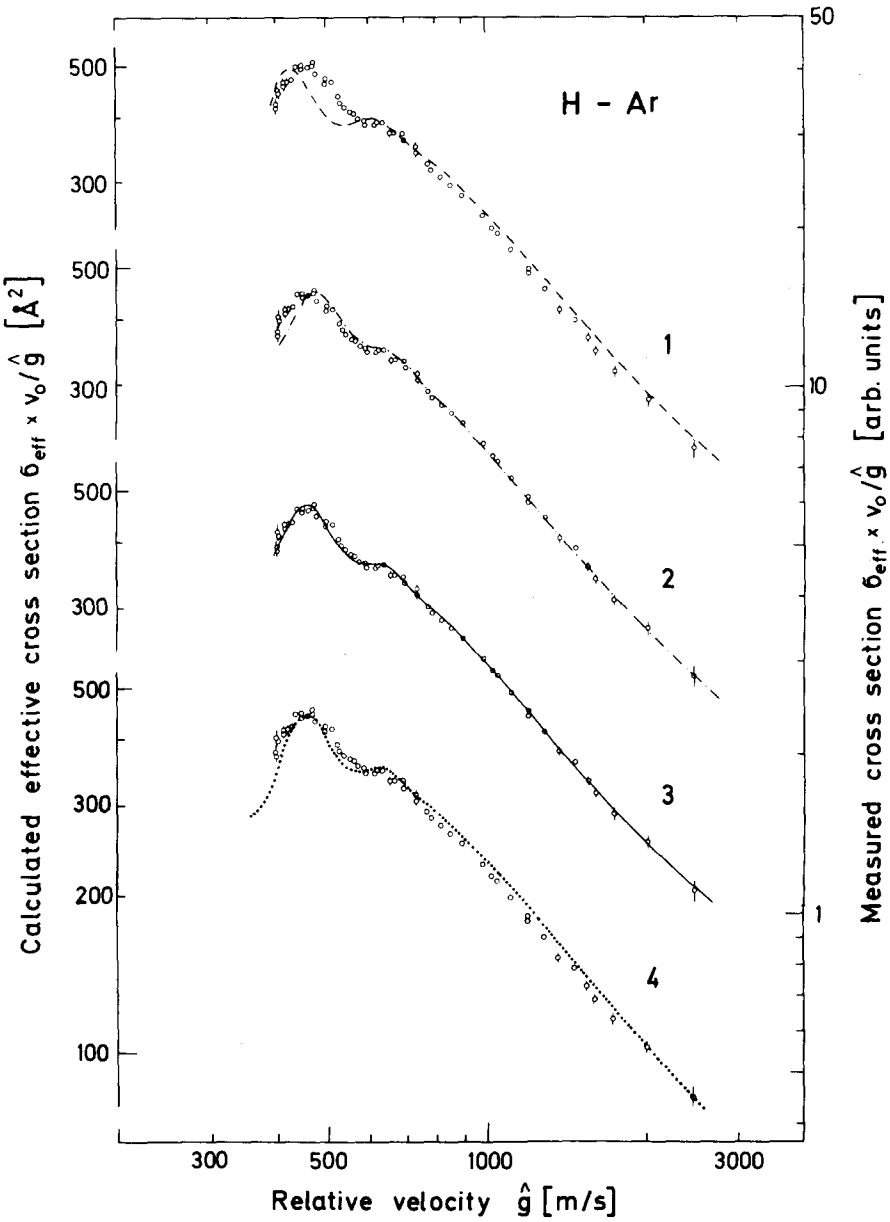

FIG. 18. The velocity dependence of cross sections calculated (left ordinate) for various potential models for H–Ar are each compared with the present measurements of relative cross sections (right ordinate). The potential models are described in Table III and plotted in Fig. 17. The experimental cross sections have been shifted slightly in the vertical direction in order to provide a best fit of the data.

D. Potentials for H_2-Ar, Kr, and Xe

Being a stable species the H_2 potential with the rare gases has received considerably more experimental attention than the H-atom rare gas potentials. Because of the additional complication presented by the anisotropy *ab initio* calculations are only available for He–H_2 and Ne–H_2. Helbing *et al.*[62] have measured the integral cross sections in the energy range $2 \leq E_{c.m.} < 100$ meV. Subsequently, Bickes *et al.*[63a] have measured the differential cross sections for H_2–Ar and Kr at 70 meV. Very recently these measurements have been repeated at two energies (17 and 65 meV) with improved resolution and new potentials have been proposed.[63b] As with the corresponding measurements of Bassi *et al.*[53] the differential scattering experiments are most sensitive to the range parameter R_0. Additional important experimental information on the spherically symmetric and ansiotropic potentials comes from the analysis of infrared pressure induced spectra of the H_2–rare gas complexes measured by Welsh and co-workers.[64] The first analysis of Le Roy and van Kranendonk[65] has been supplemented by the work of Dunker and Gordon.[66] The most recent and refined analysis of Le Roy and Carley[67,68] now supersedes this earlier work.

In Sec. IV C we presented experimental evidence that our measurements are only sensitive to the spherical symmetric part of the potential. This result is also consistent with the spectroscopic observations. Here the anisotropy leads to a coupling of the rotational motion of the molecule with the rotation of the entire complex and splitting of the energy levels. The spectra show that the splitting decreases with increasing orbital angular momentum quantum number l for the rotation of the entire complex. Thus McKellar and Welsh[64] were not able to resolve the splitting for $l > 4$ in H_2–Ar, $l > 6$ in H_2–Kr, and $l > 9$ H_2–Xe. Reference to Table I indicates that the lowest l values seen in these experiments correspond to 8, 9, and 11 (10?), respectively. The small

TABLE IV. Potential models for H–Kr.

Designation	Model	Parameters	Source	Reference	Goodness of fit: χ^{2} [b]
1	LJ(12,6) and exp(α,6)	$\epsilon = 5.99(^{+0.29}_{-0.20})$ [c] $R_m = 3.67(^{+0.32}_{-0.28})$	integral cross sections measured at $v < 18$ 10^3 m/sec	Bickes *et al.*[44]	4065
2	LJ(12,6) $R < R_s$ [d] $-\frac{C_6}{R^6} - \frac{C_8}{R^8} - \frac{C_{10}}{R^{10}}$ $R \geq R_s$	$\epsilon = 5.90$ meV $R_m = 3.57$ $R_s = 4.83$ $C_6 = 17.1 \times 10^3$ [e] $C_8 = 96.0 \times 10^3$ [f] $C_{10} = 695.2 \times 10^3$ [f]	best fit	present	345
3	WDW1[g]	$a = 150\,335$ $b = -62\,869.2$ $c = 6569.6$ $\alpha = 1.984\,21$ $d = 9200.08$ $f = 43\,244.2$ $g = 3194.56$ $\beta = 1.681\,85$ $h = 770\,663$ $\gamma = 3.460\,31$ $\epsilon = 6.1896$ $R_m = 3.70$ $R_I = 2.646$	pseudopotential MCSCF	Das *et al.*[54b]	4317

[a] All parameters are in units of meV and Å.
[b] See footnote b of Table III.
[c] See footnote b of Table II.
[d] This potential is very similar to an HFD potential communicated to us by G. Scoles.
[e] Taken from Ref. 58.
[f] Taken from Ref. 59.
[g] See Table II for the analytic expression.

effect of the anisotropy is also corroborated by a theoretical study undertaken by Schaefer[69] on the system H_2–Ar. He calculated the elastic cross section for ortho-H_2–Ar using a realistic anisotropic potential in a close-coupling calculation with a basis set including the rotational states $j = 1$, 3, and 5. Thus virtual transitions (inelastic transitions are energetically forbidden since they require 73 meV for o-H_2) were possible and might be expected to affect the velocity dependence. The results showed that such effects were negligibly small in ortho-H_2. In para-H_2 ($j = 0 \rightarrow 2$: $\Delta E_{rot} = 44$ meV) however at velocities below about 500 m/sec the effect is noticeable leading to a small shift in the resonances by about only 0.1 meV. In view of this extensive evidence from different independent sources we feel quite confident that our results can be interpreted in terms of a spherically symmetric potential. Inelastic processes for the p-H_2 component can also be neglected since the inelastic cross sections have been investigated experimentally[70] and estimated[71] to be small at energies below about 100 meV.

We now discuss each of these systems in turn:

1. H_2–Ar

The four most recent potentials are summarized in Table VI and plotted in Fig. 23. Figure 24 compares calculated cross sections with the measurements. It is seen that although the previous experimen-

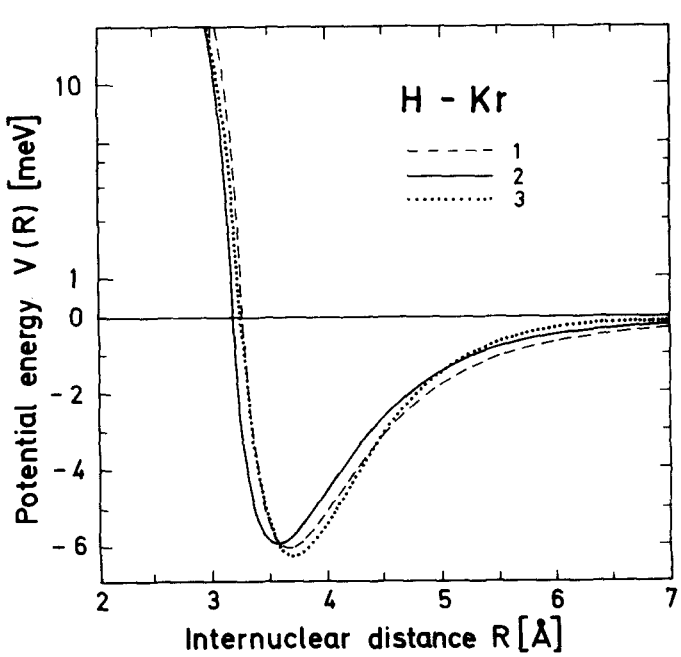

FIG. 19. Experimental and theoretical potentials for H–Kr are plotted as a function of the internuclear distance. The potential 1 is from the only previous beam experiment. Potential 2 is a best fit potential based on the theoretical values for the long range dispersion constants. Potential 3 is calculated from a pseudopotential variant of the MCSCF method. For details on these potentials see Table IV.

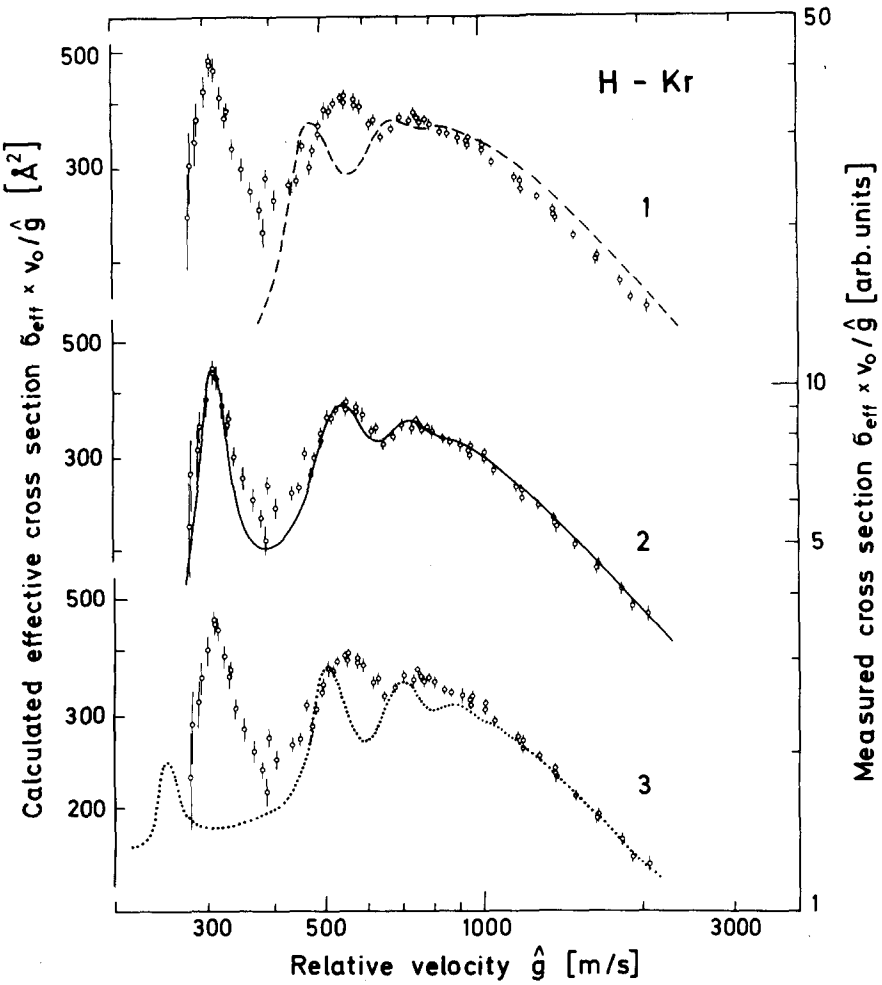

FIG. 20. The velocity dependence of cross sections calculated (left ordinate) for various potential models for H–Kr are each compared with the present measurements of relative cross sections (right ordinate). The potentials are described in Table IV and plotted in Fig. 19. The experimental cross sections have been shifted slightly in the vertical direction in order to provide a best fit of the data, because no experimental absolute cross sections are available.

TABLE V. Potential models for H–Xe.

Designation	Model	Parameters[a]	Source	Reference	Goodness of fit χ^2[b]
1	LJ(12,6)	$\epsilon = 6.65$ $R_m = 3.82$	best fit	present	555
2	LJ(12,6) $R < R_s$ $-\frac{C_6}{R^6} - \frac{C_8}{R^8} - \frac{C_{10}}{R^{10}}$ $R \geq R_s$	$\epsilon = 7.08$ $R_m = 3.82$ $R_s = 4.74$ $C_6 = 25.93$[c] $C_8 = 157.73$[d] $C_{10} = 1325.32$[d]	best fit	present	304
3	WDW 1[e]	$a = 153\,916$ $b = -61\,152.2$ $c = 6234.86$ $\alpha = 1.851\,93$ $d = 27\,468.9$ $f = 50\,579.7$ $g = 6178.73$ $\beta = 1.795\,23$ $h = 17\,924\,800$ $\gamma = 4.354\,95$ $\epsilon = 6.9128$ $R_m = 3.86$ $R_1 = 3.17$	pseudopotential MCSCF	Das *et al.*[54b]	2146

[a]All parameters are in units of mev and Å.
[b]See footnote b of Table III.
[c]Taken from Ref. 59.
[d]Taken from Ref. 60.
[e]See Table II for the analytic expression.

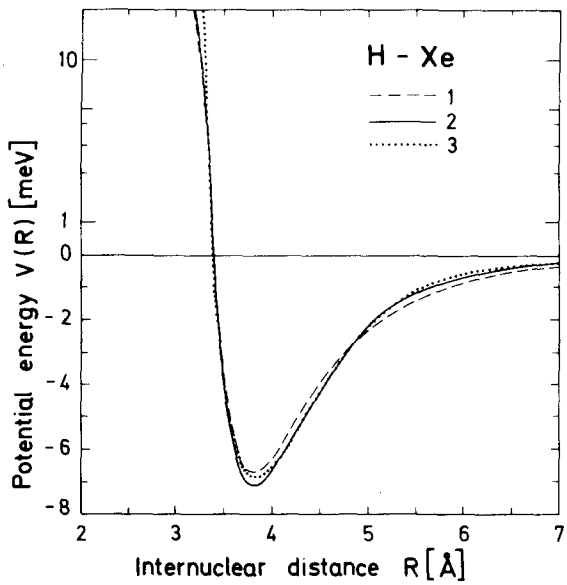

FIG. 21. Experimental and theoretical potentials for H–Xe are plotted as a function of the internuclear distance. The potential 1 is slightly modified from the only previous beam experiment. Potential 2 is a best fit potential based on the theoretical values for the long range dispersion constants. Potential 3 is calculated from a pseudopotential variant of the MCSCF method. For details on these potentials see Table V.

tal potentials predict the glory maximum from which potential 1 was derived fairly well both fail to predict the orbiting structure. The potential 3 based on infrared spectra and therefore containing information on resonances at energies below those of the orbiting resonances comes closer to the orbiting structure, but fails to reproduce the glory maximum. The most recent infrared potential 4 reproduces both types of structure best of all four potentials. From Fig. 23 we see that potentials 3 and 4 differ only slightly with regard to their shape at long distances. This small difference has a significant effect, however, on both the location of the glory and orbiting maxima as seen in Fig. 24. Recently it has been shown that potential 4 also provides an excellent fit of the new differential scattering data of Rulis *et al.* [63b] Since this potential is also in good agreement with the orbiting data, no attempt was made to find a better potential. It is gratifying to see that for this system spectroscopic, differential scattering, and orbiting data are now consistent with one and the same potential.

2. H_2–Kr

Table VII summarizes the potentials considered and Fig. 25 compares their shapes. Figure 26

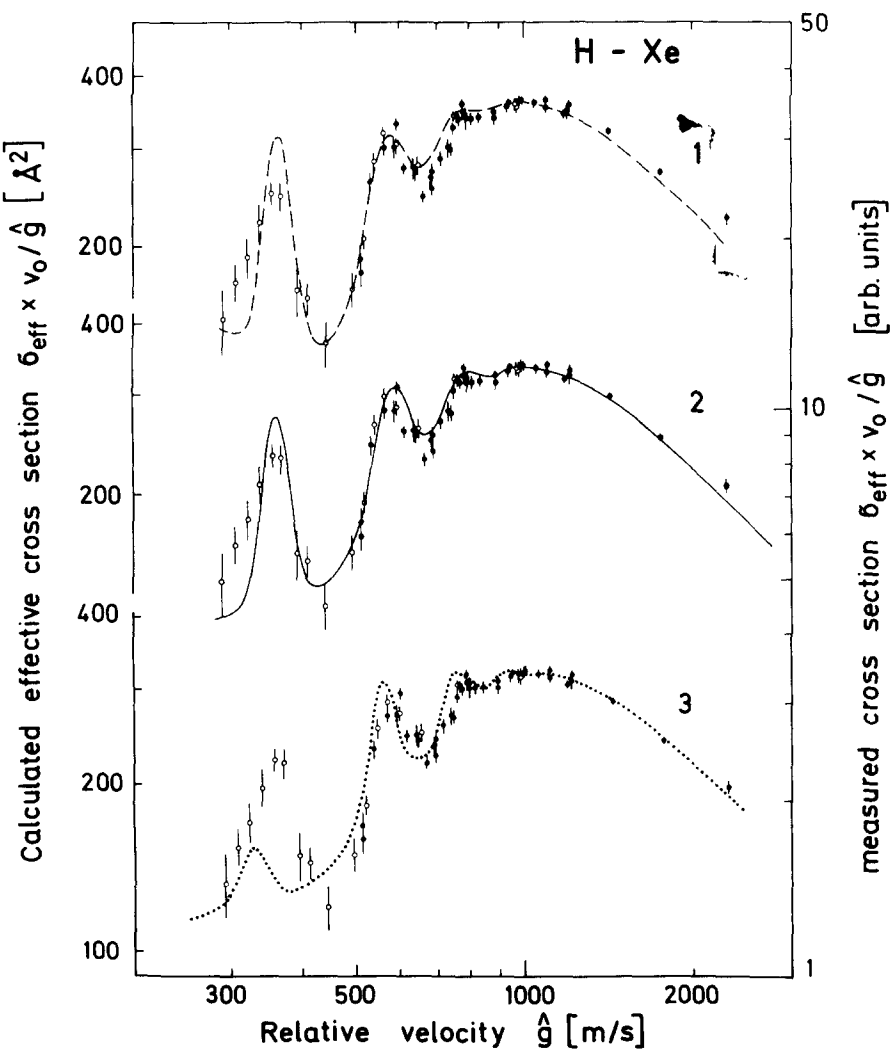

FIG. 22. The velocity dependence of cross sections calculated (left ordinate) for various potential models for H–Xe are each compared with the present measurements of relative cross sections (right ordinate). The potential models are described in Table V and plotted in Fig. 21. The experimental cross sections have been shifted slightly in the vertical direction in order to provide a best fit of the data.

TABLE VI. Models for the spherically symmetric part of the H_2–Ar potential.

Designation	Model	Parameters[a]	Source	Reference	Goodness of fit: χ^2 [b]
1	LJ(12,6)	$\epsilon = 6.305$ $R_m = 3.34$	integral cross sections measured at $v > 400$ m/sec	Helbing *et al.*[62]	1585
2	LJ(12,6)	$\epsilon = 6.11\ (\pm 0.37)$[c] $R_m = 3.44\ (\pm 0.05)$	differential cross section measurements at $E_{c.m.} = 70$ meV	Bickes *et al.*[63]	1450
3	LJ(12,6)	$\epsilon = 6.473\ (\pm 0.05)$[c] $R_m = 3.557\ (\pm 0.005)$	analysis of pressure induced infrared spectra	Le Roy and von Kranendonk[65]	1550
4	Buckingham–Corner[d]	$\epsilon = 6.303\ (\pm 0.06)$ $R_m = 3.574\ (\pm 0.005)$ $A = 3.54 \times 10^6$ $\beta = 3.692$ $C_6 = 16.912 \times 10^3$ $C_8 = 1.27 \times 10^5$ $a = 4$ $b = 1$ $c = 3$	analysis of pressure induced infrared spectra	Le Roy *et al.*[67]	531

[a]All parameters are in units of MeV and Å.
[b]See footnote b of Table III.
[c]See footnote b of Table II.
[d]This potential has the following form:

$$V(R) = A \exp(-\beta R) - \left[\frac{C_6}{R^6} + \frac{C_8}{R^8}\right] D(R),$$

where $D(R) = \exp\{-a(b/x - 1)^c\}$ for $R < b R_m$ and $D(R) = 1$ for $R \geq b R_m$.

shows a comparison of calculated cross sections with measured cross sections. As was to be expected potential 1 based on integral cross sections describes the glory maximum and the resonance at 500 m/sec reasonably well. It fails, however, in fitting the resonance at 400 m/sec. The potential 2 based on the first reported[63a] diffraction oscillations is less satisfactory. The new diffraction data[63b] is consistent with potential 3, derived from an early analysis of infrared spectroscopic data. This potential is also not able to explain either the glory structure or the orbiting maxima. In view of this situation we searched for a potential which would provide a better fit. Since the dispersion constants C_8 and C_{10} are not available for these systems the combination of a LJ (12, 6) potential with the three term dispersion series at long distances, which proved to be so successful in explaining the H–Kr and H–Xe measurements, could not be used. The simplest improvement of the LJ (12, 6) potential is achieved by using the LJ (12, 6, 8) potential.[72] In this model an additional long range C_8 term is introduced in such a way that the well depth ϵ and location R_m are unaffected. Since the reduced C_8 term given by the constant γ (for the potential formula see footnote d of Table VII) affects both the long and short range parts we gave the model additional flexibility by using different γ values for R greater than and smaller than R_m. As seen from Fig. 26 this model, designated 4, is able to provide a much better fit of the data. This new potential does not appear to be sufficiently flexible, however, to describe the orbiting structure in all respects. Note for example that the spacing of the orbiting resonances at 500 and 650 m/sec is apparently still not correctly predicted. A further improvement in the fit should be possible once a C_{10} term becomes available.[73]

Very recently Carley[68] has reported a new potential,

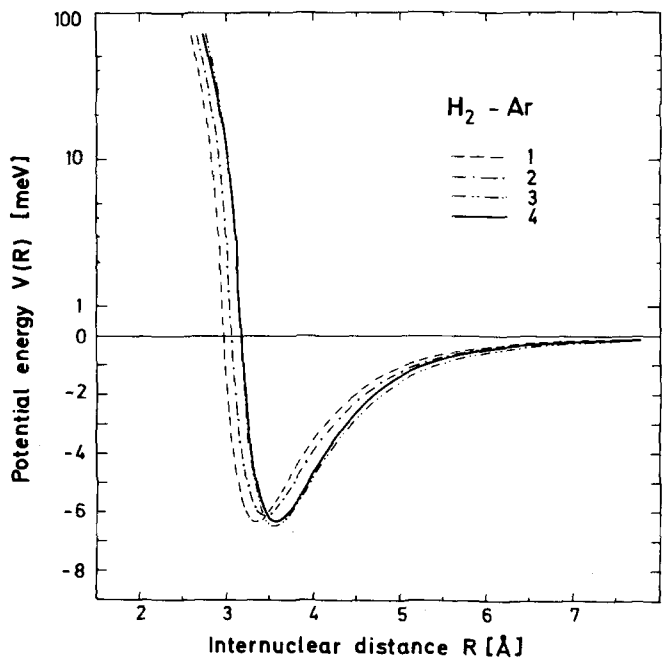

FIG. 23. Experimental isotropic potentials for H_2–Ar are plotted as a function of the internuclear distance. The potentials 1 and 2 are from beam studies at higher energies. The potentials 3 and 4 are from an analysis of pressure induced infrared spectra. The potential 4 provides a best fit of the data.

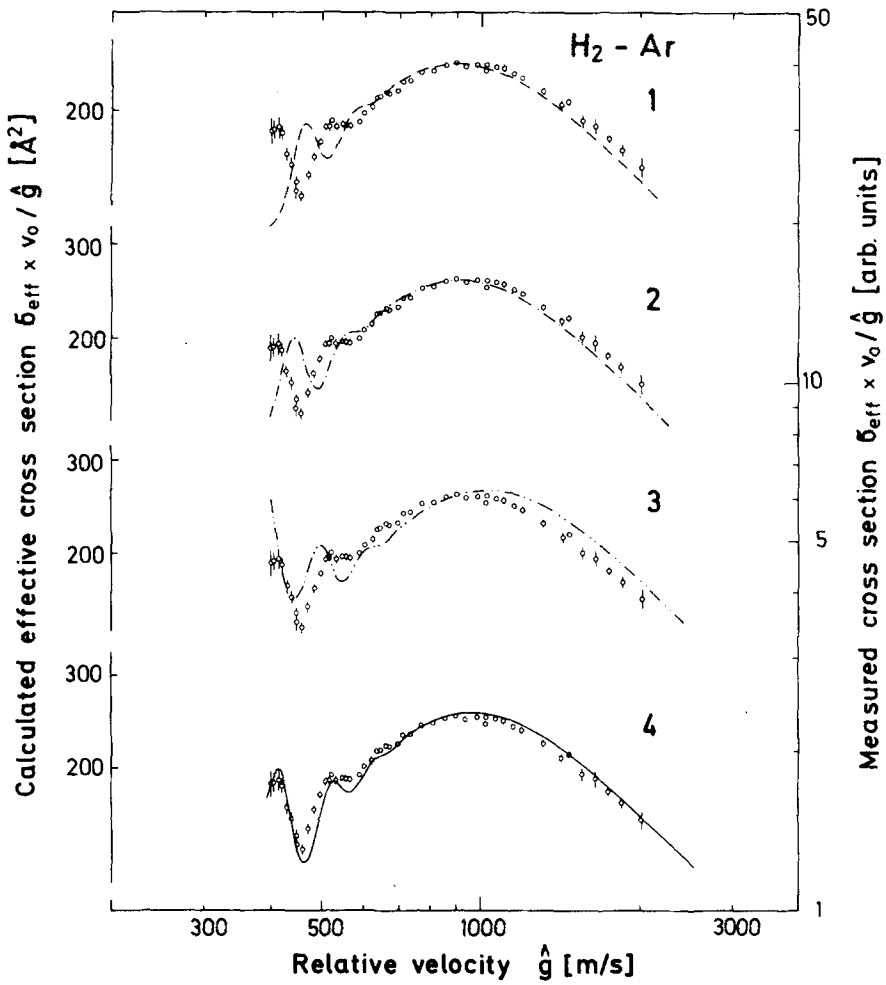

FIG. 24. The velocity dependence of elastic cross sections calculated (left ordinate) for various potential models for H_2–Ar are each compared with the present measurements of relative cross sections (right ordinate). The potentials are described in Table VI and plotted in Fig. 23.

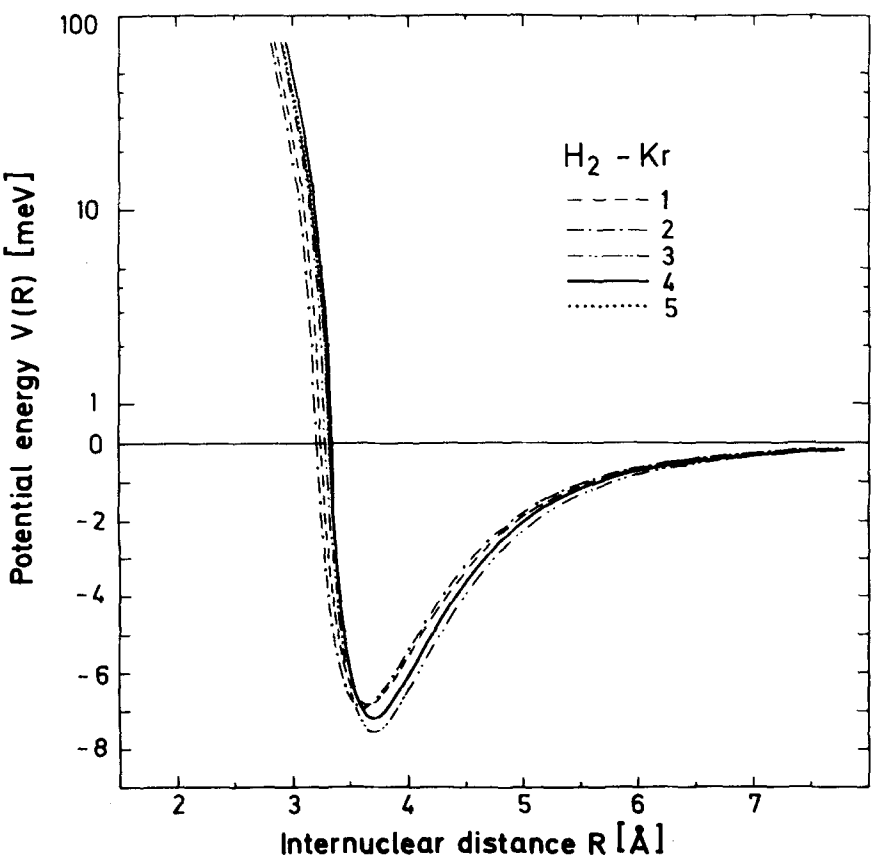

FIG. 25. Experimental isotropic potentials for H_2–Kr are plotted as a function of the internuclear distances. The potentials 1 and 2 are best fit Lennard-Jones (12, 6) models obtained from previous beam experiments at higher energies. The potential 3, which is also a Lennard-Jones (12, 6) model, was obtained from an analysis of pressure induced infrared spectra. The potential 5 is a Buckingham–Corner potential which was fitted to the same data. Potential 4 is a best fit Lennard-Jones (12, 6, 8) potential. Potentials 4 and 5 are indistinguishable except in the repulsive region.

TABLE VII. Models for the spherically symmetric part of the H_2–Kr potential.

Designation	Model	Parameters[a]	Source	Reference	Goodness of fit: χ^2 [b]
1	LJ(12,6)	$\epsilon = 6.804$ $R_m = 3.65$	integral cross sections measured at $v > 400$ m/sec	Helbing *et al.*[62]	528
2	LJ(12,6)	$\epsilon = 6.88\ (\pm 0.36)$[c] $R_m = 3.61\ (\pm 0.04)$	differential cross sections measured at $E_{c.m.} = 70$ meV	Bickes *et al.*[63]	723
3	LJ(12,6)	$\epsilon = 7.526\ (\pm 0.04)$ $R_m = 3.7014\ (\pm 0.004)$	analysis of pressure induced infrared spectra	Le Roy and van Kranendonk[65]	5870
4	LJ(12,6,8)[d]	$\epsilon = 7.19$ $R_m = 3.72$ $\gamma\left(=\frac{C_8}{\epsilon R_m^8}\right) = 2.0,\ R \le R_m$ $\gamma = 0.9,\ R > R_m$	best fit	present	127
5	Buckingham–Corner[e]	$\epsilon = 7.285\ (\pm 0.05)$ $R_m = 3.719\ (\pm 0.004)$ $A = 3.216 \times 10^6$ $\beta = 3.462$ $C_6 = 24.08 \times 10^3$ $C_8 = 2.351 \times 10^5$ $a = 4$ $b = 1$ $c = 3$	analysis of pressure induced infrared spectra	Carley[68]	440

[a] All parameters are in units of meV and Å.
[b] See footnote b of Table III.
[c] See footnote b of Table II.
[d] This potential is defined by

$$V(R) = \epsilon[(1+\gamma/3)x^{12} - 2(1-\gamma/3)x^6 - \gamma x^8],$$

where

$$x = R_m/R \quad \text{and} \quad \gamma = \frac{C_8}{\epsilon R_m^8}.$$

For $\epsilon = 7.19$ and $R_m = 3.72$, $C_6 = 26.67 \times 10^3$ and $C_8 = 2.373 \times 10^5$.
[e] See footnote d of Table VI:

$$\frac{C_8}{\epsilon R_m^8}.$$

designated 5, which he derived from the same spectroscopic data on which potential 3 is based. The R_m value of this new potential agrees within the error of 0.1% with that of the best fit potential and ϵ is only slightly larger by a mere 1.4%. This new potential provides nearly as good a fit of the measurements as the best fit potential 4 (see Fig. 26 and the χ^2 value in Table VII). The good agreement between these two potentials derived independently using different potential models is very gratifying. It demonstrates once more that the two very different techniques of spectroscopy based mostly on bound states and scattering based largely on quasibound states yield one and the same potential curve.

3. H_2–Xe

Of all the H_2–rare gas systems probably the least is known about H_2–Xe. Up to 1978 the only previous beam study of the isotropic potential was the measurement of the velocity dependence of integral cross sections reported by Helbing *et al.* This potential is designated by 1. Infrared spectra are also available and as with H_2–Kr have been interpreted by two groups to yield potentials 2 and 4. Potential 3, our best fit potential, is a two piece Lennard-Jones (12, 6, 8) potential similar to the one used for H_2–Kr. Diffraction scattering has very recently been used to study this system as well.[63b] The potentials 1, 2, 3, and 4 mentioned above, have been found to be quite consistent with these new data. However, a slightly better fit of the new diffraction results was achieved with a larger value of $R_m = 4.00$ Å instead of 3.90 ± 0.01 Å in all the potentials tested here. This potential is referred to as potential 5. The potential parameters are summarized in Table VIII and the potential shapes are shown in Fig. 27. The calculated cross sections for all potentials are compared with the measurements in Fig. 28. Potential 1 appears to provide a fairly good fit of the data. The noticeable differences seen in Fig. 28 to the experimental data are removed by the introduction of the C_8 term in

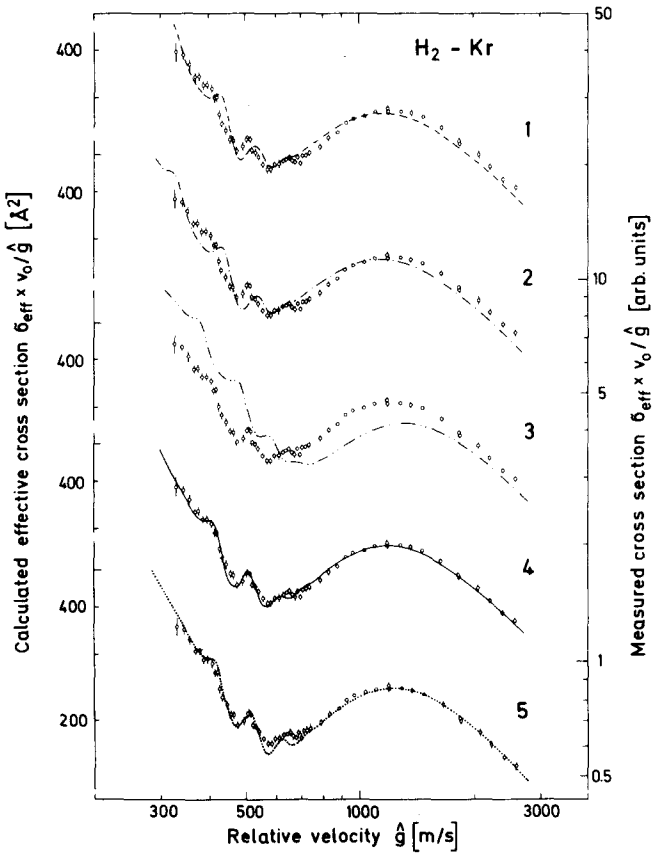

FIG. 26. The velocity dependence of elastic cross sections calculated (left ordinate) for various potential models for H_2–Kr are each compared with the present measurements of relative cross sections (right ordinate). The potentials are described in Table VII and plotted in Fig. 25.

the best fit potential 3, which at the same time has a noticeable effect on the ϵ value. The potential 4 derived from spectroscopy, agrees well with the best fit values of ϵ and R_m with a deviation of less than 0.5%. Surprisingly potential 5 also provides a very good fit of the data even though it noticeably differs in shape from potentials 3 and 4. It seems that a better resolution of orbiting resonances might well be possible for this system and will lead to an improved potential.

VI. DISCUSSION AND CONCLUSIONS

The previously discussed potential determinations are summarized in Fig. 29, which compares the potentials for all the H–rare gas systems, and Fig. 30, which compares all the potentials for the H_2–rare gas systems. A comparison between the potentials in the two sets of results yields some interesting similarities and differences. For example it is surprising to find that the potentials H–Xe and H_2–Xe are nearly identical. Moreover the R_m values are almost the same for both sets of systems. On the other hand for the H-atom interactions ϵ changes much more as the rare gas atom gets lighter than for the H_2 interactions. The small change in ϵ for different rare gas atoms has also been observed for He–rare gas atom interactions.[74] These differences appear to be related to the fact that R_0 is much the same for all the H–rare gas systems (with the exception of H–Xe) but changes systematically for the H_2–rare gas systems.

Insight into the origin of these characteristic differences is provided by the semiclassical potential model recently proposed by Tang and Toennies.[58c] This model is able to predict the well depths and location of both

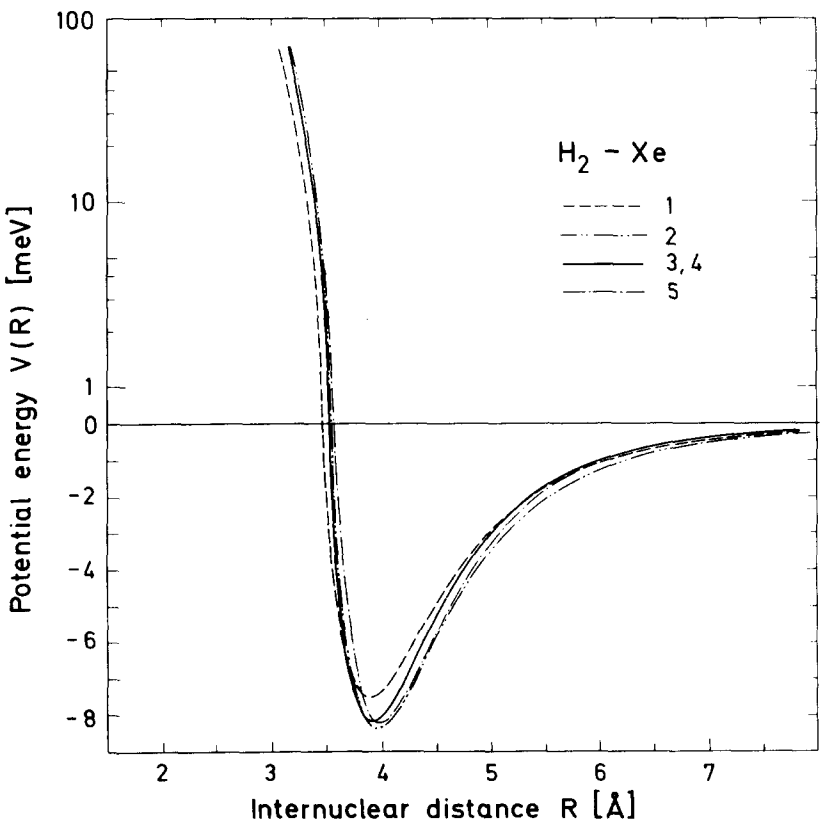

FIG. 27. Experimental isotropic potentials for H_2–Xe are plotted as a function of the internuclear distances. The potential 1 is a Lennard–Jones (12, 6) potential fitted to integral cross section measurements. The potentials 2 and 4 are from an analysis of pressure induced infrared spectra. Potential 3 is a best fit Lennard–Jones (12, 6, 8) potential, which is indistinguishable from potential 4.

TABLE VIII. Models for the spherically symmetric part of the H_2–Xe potential.

Designation	Model	Parameters[a]	Source	Reference	Goodness of fit: χ^2[b]
1	LJ(12,6)	$\epsilon = 7.43$ $R_m = 3.90$	integral cross sections measured at $v > 400$ m/sec	Helbing *et al.*[62]	992
2	LJ(13,6)	$\epsilon = 8.311$ (± 0.05)[c] $R_m = 3.9214$ (± 0.004)	analysis of pressure induced infrared spectra	Le Roy and van Kranendonk[65]	5042
3	LJ(12,6,8)[d]	$\epsilon = 8.10$ $R_m = 3.92$ $\gamma \left(= \frac{C_8}{\epsilon R_m^8}\right) = 2.0 \quad R \leq R_m$ $\gamma = 1.2 \quad R > R_m$	best fit	present	270
4	Buckingham–Corner[e]	$\epsilon = 8.117$ $R_m = 3.934$ $A = 12.32 \times 10^6$ $\beta = 3.668$ $C_6 = 40.98 \times 10^3$ $C_8 = 2.147 \times 10^5$ $a = 4$ $b = 1$ $c = 3$	analysis of pressure induced infrared spectra	Carley[68]	226
5	HFD[f]	$\epsilon = 8.18$ $R_m = 4.00$ $A = 19.27 \times 10^7$ $\beta = 3.768$ $C_6 = 40.955 \times 10^3$ $C_8 = 2.064 \times 10^5$ $C_{10} = 14.998 \times 10^5$ $a = 1.00$ $b = 1.28$ $c = 2.00$	differential cross sections measured at $E_{c.m.} = 17$ and 68 meV.	Rulis *et al.*[62b]	226

[a]All parameters are in units of meV and Å.
[b]See footnote b of Table III.
[c]See footnote b of Table II.
[d]See footnote d of Table VII. For $\epsilon = 8.10$ and $R_m = 5.92$, $C_6 = 35.27 \times 10^3$, and $C_8 = 2.623 \times 10^5$.
[e]See footnote d of Table IV.
[f]Same as the Buckingham-Corner potential but with different parameters a, b, c and an additional $-C_{10}R^{-10}$ term.

closed shell–closed shell and open shell–closed shell systems. The only necessary input data are theoretical SCF Born–Mayer parameters A and b [$V(R) = A \exp(-bR)$] and perturbation theory dispersion constants up to high order, typically R^{-12} or even higher depending on the system. The same differences in behavior in ϵ and R_m noted above are also found in comparing the two sets of open shell systems M–Ne, Ar for M = Li and M = Na with the closed shell systems He–Ne and He–Ar. For these systems all the input data[75] are available and therefore it is possible to understand the differences in terms of the Tang–Toennies model. For the closed shell systems the repulsive range parameter is typically very large and dispersion terms up to high order contribute. Thus for these systems the potentials are best described by a hard core and sharply attractive potential as in the simple Sutherland model. For this reason chemical differences in C_6, which contributes little at R_m, have little effect on ϵ.

In the open shell systems the repulsive range parameters are much smaller and the repulsive potential is therefore "softer." Moreover only few terms in the dispersion series contribute. At most only the R^{-6} and R^{-8} terms contribute for the above mentioned systems. This leads one to expect much rounder potential bowls. In this case differences in the strength of the C_6 term have a proportionally large effect on ϵ. This explanation should also hold for the H– and H_2–rare gas systems and the expected differences are also seen in comparing Fig. 29 with Fig. 30. A study of the systems H_2–Ar, Kr, and Xe based on theoretical parameters derived from combining rules using the Tang–Toennies model is in progress[73] and will make it possible to explain the chemical differences observed for H and H_2 in more detail.

A close examination of Fig. 29 indicates that H–Kr departs significantly from the trend in the R_m values expected in going from Ne, Ar, Kr, Xe. This rather surprising result apparently has to do with subtle differences in the C_6 and Born–Mayer parameters which as discussed above are important in the open shell systems.

The analysis of orbiting structures and the extensive

comparisons presented in this paper show that orbiting structures provide an extremely sensitive probe of van der Waals forces.

From the data it is possible to determine both ϵ and R_m if a sufficiently realistic potential model is used. The results are particularly sensitive to the exact shape of the long range potential. The six examples considered show that in all cases the agreement was improved if at least an C_8R^{-8} term was included in the long range expansion. In the case of H–Kr and H–Xe where the resonance maxima were most pronounced the inclusion of a calculated term C_{10} was necessary and gave very good agreement. The accuracy and reliability of potentials determined from orbiting was confirmed by the excellent agreement found between our potentials for H_2–Kr and H_2–Xe and those found independently from an analysis of infrared spectra. The advantage of orbiting is that it is not restricted to closed shell systems.

Including the recent orbiting results for H–Hg,[22] He–Ne,[25] H–CF_4,[24d] and H–SF_6[24d] altogether ten systems have have now been studied by this method. In all cases so far only light primary beams have been used. Although

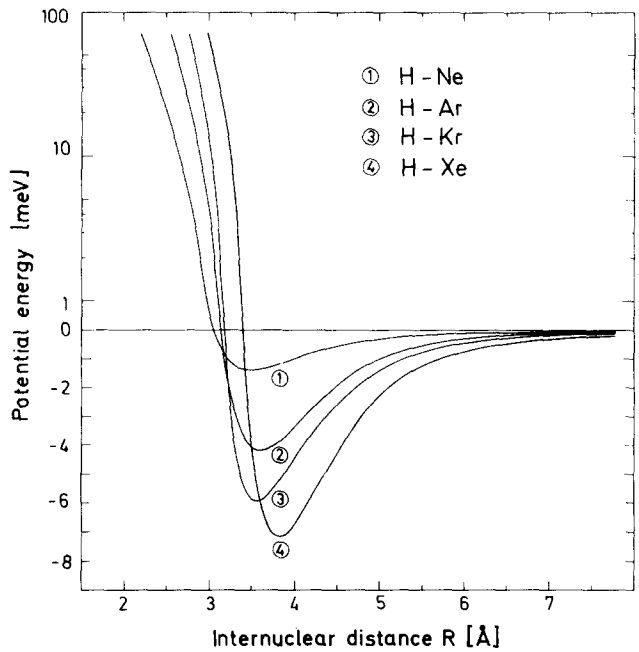

FIG. 29. The best fit potential established from a comparison with the present low energy cross section measurements for the interaction of H atoms with Ne, Ar, Kr, and Xe are compared. Note that the well minimum location from the system H–Kr deviates from that expected from the other systems.

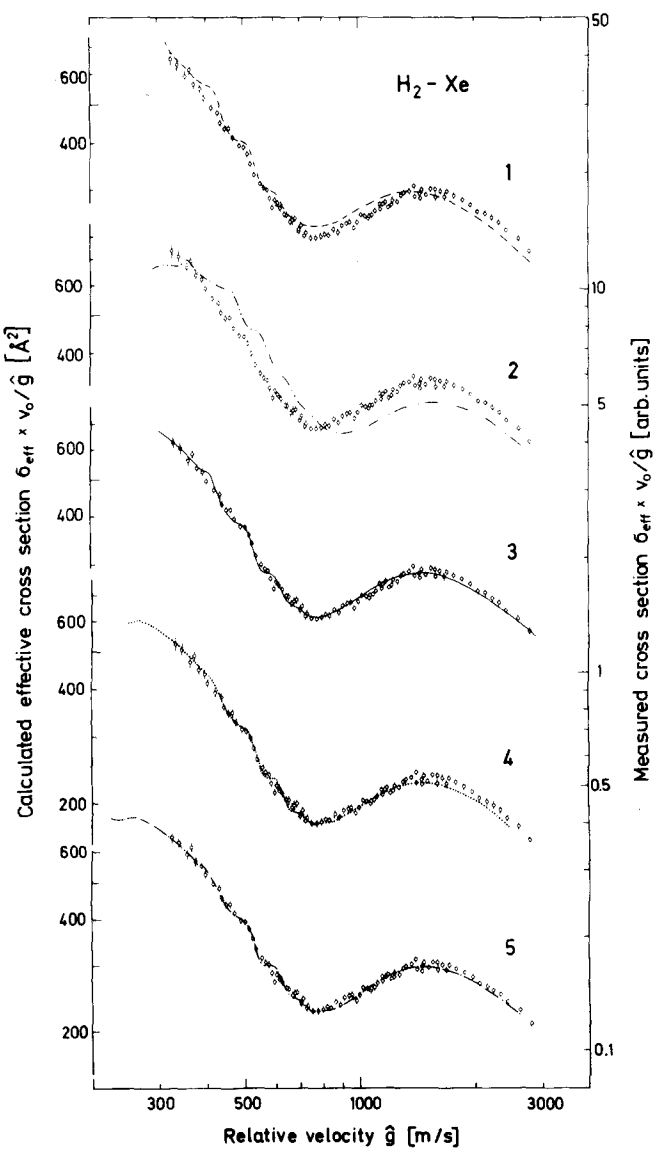

FIG. 28. The velocity dependence of elastic cross sections calculated (left ordinate) for various potential models for H_2–Xe are each compared with the present measurements of relative cross sections (right ordinate). The potentials are described in Table VIII and plotted in Fig. 27.

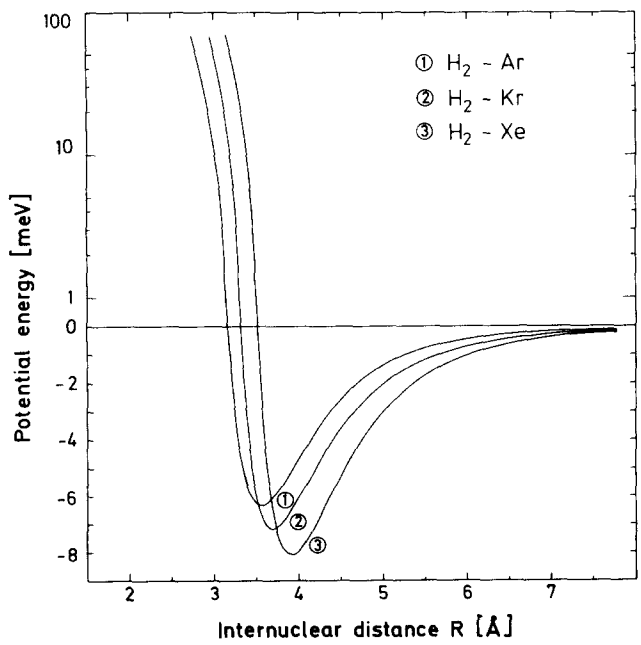

FIG. 30. The best fit potentials established from a comparison with the present low energy cross section measurements for the interaction of H_2 molecules with Ar, Kr, and Xe are compared. Note that all three systems have very similar shapes and nearly equal well depths.

the same phenomena are expected in the scattering of heavier atoms and molecules the resonances are generally much narrower and more difficult to resolve.[76] Thus at the present time the technique of studying potentials using measured orbiting maxima is restricted to light systems. But here it is probably the most reliable and precise single method available for studying van der Waals potentials.

Strongly anisotropic systems present special problems in their interpretation. Whereas no resonances could be found for $H-O_2$,[78] which is known to have a deep "chemical" well with a large anisotropy, orbiting resonances have very recently been seen in H–HCl, H–HBr, and H–HI.[77] In the seemingly very anisotropic system $H-C_2H_4$ a resonance type structure has been observed which so far has not been explained.[78]

ACKNOWLEDGMENTS

This article is dedicated to Professor W. Hartmann on the occasion of his 65th birthday in grateful acknowledgment of his active enthusiastic support of the study of chemical elementary processes in Germany.

We are very thankful to R. J. Le Roy (Waterloo) for both communicating his results on the H_2–rare gas systems prior to publication and for many valuable comments on the draft manuscript. We thank G. Das, Al. Wagner, and A. C. Wahl (Argonne Labs) for keeping us informed on the progress of their calculations and G. Scoles (Waterloo) for sending us his HFD potential for H–Kr and H_2–Xe. We also thank J. Schaefer (Munich) for performing close coupling calculations on H_2–Ar. We are grateful for the help of U. Schwalm and K. Müller in carrying out some of the cross section comparisons. The apparatus was designed in collaboration with A. Sauer. Technical assistance during the measurements was provided by G. Redlich and H. Wuttke. We thank them and the members of the shop for their skillful help which made these difficult experiments possible.

[1]L. Boltzmann, *Vorlesung über Gastheorie*, Vol. II (J. A. Barth, Leipzig, 1898), p. 186.
[2]K. F. Herzfeld, Z. Phys. **8**, 132 (1922).
[3]W. Steiner, Z. Phys. Chem. B **15**, 249 (1932).
[4]R. C. Tolman, *Statistical Mechanics with Applications to Physics and Chemistry* (Oxford University, London, 1927), p. 245–297.
[5]J. O. Hirschfelder, C. F. Curtiss, and R. B. Bird, *Molecular Theory of Gases and Liquids* (Wiley, New York, 1954).
[6]K. W. Ford, D. L. Hill, M. Wakano, and J. A. Wheeler, Ann. Phys. **7**, 239 (1959). See also B. C. Eu and J. Ross, J. Chem. Phys. **44**, 2467 (1966).
[7]D. L. Bunker, J. Chem. Phys. **32**, 1001 (1960).
[8]R. E. Roberts, R. B. Bernstein, and C. F. Curtiss, J. Chem. Phys. **50**, 5163 (1969); P. A. Whitlock, J. T. Muckerman, and R. E. Roberts, J. Chem. Phys. **60**, 3658 (1974).
[9]See for example R. T Pack, R. L. Snow, and W. D. Smith, J. Chem. Phys. **56**, 926 (1972).
[10]M. von Seggern and J. P. Toennies, Z. Phys. **218**, 341 (1969).
[11]V. H. Shui and J. P. Appleton, J. Chem. Phys. **55**, 3126 (1971).
[12](a) D. W. Trainor, D. O. Ham, F. Kaufman, J. Chem. Phys. **58**, 4599 (1973); (b) D. N. Mitchell and D. J. LeRoy, *ibid.* **67**, 1042 (1977).
[13]D. E. Stogryn and J. O. Hirschfelder, J. Chem. Phys. **31**, 1531 (1958); **31**, 1545 (1959).
[14](a) W. Erlewein, M. von Seggern, and J. P. Toennies, Z. Phys. **211**, 35 (1968); (b) L. Monchik, S. Green, J. Chem. Phys. **63**, 2000 (1975); (c) J. Schaefer, private communication.
[15]G. Herzberg, *Molecular Spectra and Molecular Structure, I. Spectra of Diatomic Molecules* (Van Nostrand Reinhold, New York, 1950).
[16](a) A. R. W. McKellar and H. L. Welsh, J. Chem. Phys. **55**, 595 (1971); (b) Can. J. Phys. **50**, 1458 (1972); (c) Can. J. Phys. **52**, 1082 (1974); (d) R. J. Le Roy and J. van Kranendonk, J. Chem. Phys. **61**, 4750 (1974).
[17]For reviews see (a) R. J. Le Roy in *Specialist Periodical Reports on Molecular Spectroscopy*, Vol. 1 (The Chemical Society, Burlington House, London, 1973), p. 113, (b) M. S. Child in *Specialist Periodical Reports on Molecular Spectroscopy*, Vol. 2 (The Chemical Society, Burlington House, London, 1974), p. 466.
[18](a) R. B. Bernstein, Phys. Rev. Lett. **16**, 385 (1966); (b) O. Goscinski and O. Tapia, Mol. Phys. **24**, 641 (1972); (c) L. Gottdiener and J. N. Murrell, *ibid.* **25**, 1041 (1975).
[19]Orbiting or complex formation with and without chemical reactions has been detected in a large number of atom–molecule collision partners by the observation of angular distributions with large backward peaks. However no serious attempts were made to study these distributions as a function of energy, See, for example: (a) W. B. Miller, S. A. Safron, and D. R. Herschbach, Discuss. Faraday Soc. **44**, 108 (1967); (b) D. O. Ham and J. L. Kinsey, J. Chem. Phys. **53**, 285 (1970); (c) D. Beck and H. Förster, Z. Phys. **240**, 136 (1970); (d) J. M. Parson and Y. T. Lee, J. Chem. Phys. **56**, 4658 (1972).
[20]The ionic fragments of predissociating orbiting states of molecular ions such as $He-H^+$ have also been recently observed. See, for example: J. Schopman and J. Los, Physica **48**, 190 (1970); J. Schopman, P. G. Fournier, and J. Los, *ibid.* **63**, 518 (1973).
[21]See, for example: W. C. Stwalley, A. Niehaus, and D. R. Herschbach, *Abstracts of Papers of the* VIth *International Conference on the Physics of Electronic and Atomic Collisions* (Nauka Press, Leningrad, 1967), p. 639; F. G. Collins and F. C. Hurlbut, J. Chem. Phys. **56**, 2609 (1972).
[22](a) W. C. Stwalley, A. Niehaus, and D. R. Herschbach, J. Chem. Phys. **63**, 3081 (1975); (b) A. Schulte, D. Bassi, F. Tommasini, and G. Scoles, *ibid.* **62**, 600 (1975); (c) K. A. Köhler, R. Feltgen, and H. Pauly, Phys. Rev. A **15**, 1407 (1977).
[23]W. C. Stwalley, J. Chem. Phys. **63**, 3062 (1975).
[24]Preliminary reports on these measurements are (a) H–Xe: J. P. Toennies, W. Welz and G. Wolf, J. Chem. Phys. **61**, 2461 (1974); (b) H–Ar, Kr, Xe: J. P. Toennies, W. Welz, and G. Wolf, *Abstracts of Papers of the* IXth *International Conference on the Physics of Electronic and Atomic Collisions*, edited by J. S. Risley and R. Geballe (University of Washington, Seattle, 1975), p. 1007; (c) H_2–Ar, Kr, Xe: J. P. Toennies, W. Welz, and G. Wolf, J. Chem. Phys. **64**, 5305 (1976); (d) $H-CF_4$, SF_6: R. Grover, J. P. Toennies, W. Welz, and G. Wolf, Chem. Phys. Lett. **48**, 24 (1977).
[25]R. S. Grace, D. L. Johnson, and J. G. Skofronick, J. Chem. Phys. **67**, 2443 (1977).
[26](a) F. T. Smith, Phys. Rev. **118**, 349 (1960); Erratum: Phys. Rev. **119**, 2098 (1960); (b) R. J. Le Roy and R. B. Bernstein, J. Chem. Phys. **54**, 5114 (1971).
[27](a) J. N. L. Connor, Mol. Phys. **15**, 621 (1968); **16**, 525 (1969); **23**, 717 (1972); (b) R. R. Herm, J. Chem. Phys. **47**, 4290 (1967); (c) R. J. LeRoy and W.-K. Lin, J. Chem. Phys. (to be published).
[28]W. C. Stwalley, Abstracts of the VIII International Conference on the Physics of Electronic and Atomic Collisions,

Vol. 1, Belgrade, 1973, p. 40.
[29]At 2000 m/sec the correction amounts to $\lesssim 1.5\%$ of σ_0, see page 287ff of H. Pauly and J. P. Toennies in *Methods of Experimental Physics*, Vol. 7A (Academic, New York, 1968), pp. 227–360.
[30]See p. 283ff of Ref. 29.
[31]G. Clausnitzer, W. Dürr, R. Fleischmann, G. Graw, W. Hammon, G. Hartmann, W. Kretschmer, H. Nahr, A. Neufert, E. Salzborn, H. Wilsch, and J. Witte, Nucl. Instrum. Methods **80**, 245 (1970).
[32]H. Wilsch, J. Chem. Phys. **56**, 1412 (1974).
[33]Similar discharge sources for H atoms have been described by: (a) R. T. Brackmann and W. L. Fite, J. Chem. Phys. **34**, 1572 (1961); (b) G. O. Brink, R. A. Fluegge, and R. J. Hull, Rev. Sci. Instrum. **39**, 1171 (1968); (c) V. Aquilanti, G. Liuti, E. Luzzatti, F. Vecchio–Cattivi, and G. G. Volpi, Z. Phys. Chem. **79**, 200 (1972); (e) T. M. Miller, J. Appl. Phys. **45**, 1713 (1974); (f) A. Schalk, D. Bassi, F. Tommasini, and G. Scoles, J. Chem. Phys. **62**, 600 (1975); (g) K. A. Köhler, Dissertation, Bonn (1975).
[34]H. Wise and B. J. Wood, Adv. At. Mol. Phys. **3**, 291 (1967).
[35]The resonator is similar to one described by W. W. Mac Alpine and R. O. Schildknecht, Proc. IRE **2099** (1959).
[36]This was confirmed by several independent measurements in our laboratory carried out by U. Borkenhagen, R. David, M. Faubel, H. Malthan, and K. Winkelmann.
[37]We are grateful to G. Brusdeylins and H. D. Meyer of our laboratory for performing these measurements for us.
[38]W. Bauer, L. Y. Rusin, and J. P. Toennies, J. Chem. Phys. **68**, 4490 (1978).
[39]E. V. Kornelsen and B. Domeij, J. Vac. Sci. Tech. **3**, 20 (1966).
[40]Page 284 of Ref. 29.
[41]W. B. Miller, Dissertation Harvard University, Cambridge, MA, 1969.
[42]F. W. Dustmann, Max-Planck-Institut für Strömungsforschung, Report No. 114/1975, 1975.
[43]"See AIP document No. PAPS JCPSA-71-614-11 for 11 pages of measured relative integral cross sections with errors for different primary beam velocities in the sequential order of the measurements for all systems. Order by PAPS number and journal reference from American Institute of Physics, Physics Auxiliary Publication Service, 335 East 45th Street, New York, NY 10017. The price is $1.50 for each microfiche (98 pages), or $5 for photocopies of up 30 pages with $0.15 for each additional page over 30 pages. Airmail additional. Make checks payable to the American Institute of Physics. This material also appears in Current Physics Microform, the monthly microfilm edition of the complete set of journals published by AIP, on the frames immediately following this journal article."
[44]R. W. Bickes, Jr., B. Lantzsch, J. P. Toennies, and K. Walaschewski, Faraday Discuss. Chem. Soc. **55**, 167 (1973).
[45]See, for example, N. F. Mott and H. S. W. Massey, *The Theory of Atomic Collisions* (Clarendon Press, Oxford, 1965), p. 39.
[46]L. Zandee and J. Reuss, Chem. Phys. **26**, 345 (1977).
[47]Strictly speaking this assertion is only valid if transitions to energetically forbidden states (closed channels) are neglected. In order to explore the effect of closed channels J. Schaefer has carried out close-coupling calculations for H_2–Ar with and without closed channels using a realistic anisotropic potential. The results indicate that at the lowest energies probed in these experiments the closed channels have no effect on the cross sections confirming our assertion. However at lower collision energies closed channels do lead to a shift and broadening of the resonances.
[48]M. Faubel and J. P. Toennies, J. Chem. Phys. (to be published).
[49]G. Herzberg, *Molecular Spectra and Molecular Structure, I. Spectra of Diatomic Molecules* (Van Nostrand, New York, 1950).
[50]H. D. Meyer and J. P. Toennies (to be published).
[51]W. Welz, Max-Planck-Institut für Strömungsforschung, Report No. 107/1976, 1976.
[52]F. Calogero, *Variable Phase Approach to Potential Scattering* (Academic, New York, 1968).
[53]D. Bassi, M. G. Dondi, F. Tommasini, F. Torello, and U. Valbusa, Phys. Rev. A **13**, 584 (1976).
[54](a) G. Das, A. F. Wagner, and A. C. Wahl, private communication; (b) J. Chem. Phys. **68**, 4917 (1978).
[55]W. C. Stwalley, J. Chem. Phys. **61**, 3840 (1974).
[56]Ch. Hahn, Max-Planck-Institut für Strömungsforschung, Report No. 118/1972, 1972.
[57]A. F. Wagner, G. Das, and C. Wahl, J. Chem. Phys. **60**, 1885 (1974).
[58](a) J. P. Toennies, Chem. Phys. Lett. **20**, 238 (1973); (b) R. Ahlrichs, R. Penco, and G. Scoles, Chem. Phys. **19**, 119 (1977); (c) K. T. Tang and J. P. Toennies, J. Chem. Phys. **66**, 1496 (1977).
[59]G. Starkschall, J. Chem. Phys. **56**, 5729 (1972).
[60]W. C. Stwalley, J. Chem. Phys. **61**, 3840 (1974).
[61]The critical value of B was determined by trial and error.
[62]R. Helbing, W. Gaide, and H. Pauly, Z. Phys. **208**, 215 (1968).
[63](a) R. W. Bickes, Jr., G. Scoles, and K. M. Smith, Can. J. Phys. **53**, 435 (1975); (b) A. M. Rulis, K. M. Smith, and G. Scoles, Can. J. Phys. **56**, 753 (1978).
[64](a) A. R. W. McKellar and H. L. Welsh, J. Chem. Phys. **55**, 595 (1971); (b) **61**, 4636 (1974); (c) H. L. Welsh in *Spectroscopy* (Butterworths, London, 1972); M. T. P. International Reviews of Science, Physical Chemistry, Vol. 3, p. 83.
[65]R. J. LeRoy and J. van Kranendonk, J. Chem. Phys. **61**, 4750 (1974).
[66](a) A. M. Dunker, Ph. D. thesis, Harvard University, Cambridge, MA, 1974. Results from this thesis yielded 5%–8% larger well depths for H_2–Ar, Kr, and Xe than those found in Refs. 22 and 23 and in the present work. For this reason no detailed comparison with this work was made; (b) A. M. Dunker and R. G. Gordon, J. Chem. Phys. **68**, 700 (1978).
[67]R. J. LeRoy, J. Carley, and J. E. Grabenstetter, Faraday Discuss. Chem. Soc. **62**, 169 (1977).
[68]J. S. Carley, Faraday Discuss. Chem. Soc. **62**, 303 (1977).
[69]J. Schäfer, private communication.
[70]R. M. Jonkman, G. J. Prangsma, I. Erlas, H. F. P. Knaap, and J. J. M. Beenakker, Physica **38**, 441 (1968).
[71]L. Zandee and J. Reuss, Chem. Phys. **26**, 345 (1977).
[72]H. J. M. Hanley and M. Klein, Technical Note 628, National Bureau of Standards (USA), 1972.
[73]C_8 and C_{10} coefficients have recently been estimated for H_2–Ar, Kr, and Xe; K. T. Tang and J. P. Toennies (to be published).
[74](a) C. H. Chen, P. E. Siska, and Y. T. Lee, J. Chem. Phys. **59**, 601 (1973); (b) K. M. Smith, A. M. Rulis, G. Scoles, R. A. Aziz, and V. Nain, *ibid.* **67**, 152 (1977).
[75]For references to the original literature and a compilation of the theoretical and experimental potential parameters see Ref. 74.
[76]For calculations of Ne–Ne see J. P. Toennies and K. Winkelmann, J. Chem. Phys. **66**, 3965 (1977).
[77]U. Schwalm and J. P. Toennies, Chem. Phys. Lett. 63, 17 (1979).
[78]Lev. Y. Rusin and J. P. Toennies, *Abstracts of Papers* XIth *International Conference on Physics of Electronic and Atomic Collisions* (Commissariat à l'Energie Atomique, Paris, 1977), p. 88.